HHS Public Access

Author manuscript

Neuron. Author manuscript; available in PMC 2024 May 03.

Published in final edited form as:

Neuron. 2023 May 03; 111(9): 1486–1503.e7. doi:10.1016/j.neuron.2023.02.012.

Glutamatergic and GABAergic Neurons in Pontine Central Gray Mediate Opposing Valence-Specific Behaviors through A Global Network

Cuiyu Xiao[1,+], **Jinxing Wei**[1,+], **Guang-wei Zhang**[1], **Can Tao**[1], **Junxiang J. Huang**[1,2], **Li Shen**[1], **Ian R. Wickersham**[4], **Huizhong W. Tao**[1,3,*], **Li I. Zhang**[1,3,*,#]

[1]Zilkha Neurogenetic Institute, Department of Physiology and Neuroscience, Keck School of Medicine, University of Southern California, Los Angeles, CA 90033, USA.

[2]Graduate Program in Biological and Biomedical Sciences, University of Southern California.

[3]Center for Neural Circuits and Sensory Processing Disorders, Keck School of Medicine, University of Southern California, Los Angeles, CA 90033, USA.

[4]McGovern Institute for Brain Research, Massachusetts Institute of Technology, Cambridge, MA 02139, USA.

Summary

Extracting the valence of environmental cues is critical for animals' survival. How valence in sensory signals is encoded and transformed to produce distinct behavioral responses remains not well-understood. Here, we report that the mouse pontine central gray (PCG) contributes to encoding both negative and positive valences. PCG glutamatergic neurons were activated selectively by aversive but not reward stimuli, while its GABAergic neurons preferentially activated by reward signals. Optogenetic activation of these two populations resulted in avoidance and preference behavior respectively and was sufficient to induce conditioned place aversion/preference. Suppression of them reduced sensory-induced aversive and appetitive behaviors, respectively. These two functionally opponent populations, receiving a broad range of inputs from overlapping yet distinct sources, broadcast valence-specific information to a distributed brain network with distinguishable downstream effectors. Thus, PCG serves as a critical hub to process

*Correspondence should be addressed to: H.W.T (htao@usc.edu) or L.I.Z.(liizhang@usc.edu).
#Lead Contact
+These authors contributed equally to this work.

AUTHOR CONTRIBUTIONS

L.I.Z. and H.W.T. conceived the study and supervised the project. C.X. and J.W. carried out anatomical, in vivo recording and all behavioral experiments as well as data analysis. G.Z. helped with behavioral experiments and data analysis. J.J.H. helped with anatomy, C.T. performed slice recording, L.S. helped with recording data analysis. L.I.Z, H.W.T and I.R.W. contributed to resources. C.X., L.I.Z. and H.W.T. wrote the manuscript.

DECLARATION OF INTERESTS

I.R.W. is a consultant for Monosynaptix, LLC, advising on design of neuroscientific experiments. The other authors declare no competing interests.

positive and negative valences of incoming sensory signals and drive valence-specific behaviors with distinct circuits.

Graphical Abstract

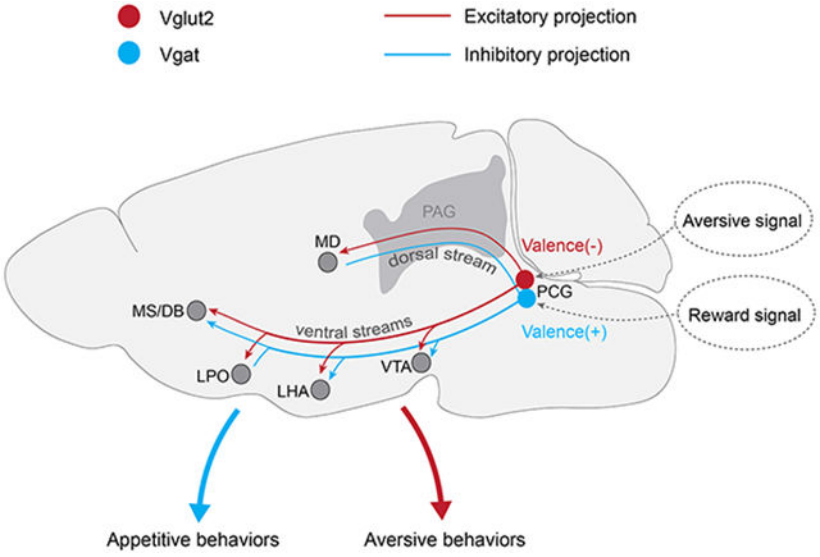

eTOC blurb

Xiao *et al.* found that pontine central gray (PCG) contributes to encoding positive and negative valences through activity of its GABAergic and glutamatergic neurons respectively, which mediate sensory-induced reward- and aversion-related behaviors. Thus, PCG may serve as a critical hub for bottom-up processing of sensory valence preceding the limbic system.

Introduction

In natural environments, animals are bombarded with barrages of sensory information. Yet they are able to filter out unimportant information and rapidly respond to the dynamic surroundings in an adaptive manner. The valence of environmental cues is defined by their associated positive or negative outcomes [1-3]. Detecting and discriminating the valence of external signals are thus essential for animals' survival and well-being. Negative valence signals usually result in avoidance/aversive behaviors, while positive valence signals result in approach/appetitive behaviors [4-7]. Although abundant previous studies have been focused on how different brain structures and cell types are involved in aversion- or reward-related emotional processing [8-18], how values of valence are extracted from incoming sensory signals and represented by neurons along the sensory processing pathways remains largely unclear.

Valence coding neurons are those exhibiting differential responses to cues associated with reward and threat/punishment, independent of modality [16-18]. Previous studies searching for valence coding neurons have identified a great number of brain regions relevant to emotional/motivational processing. These regions include the amygdala, hippocampus,

prefrontal cortex, striatum, lateral hypothalamus, habenula and various neuromodulatory systems [11,14-30] , suggesting that the valence processing framework may involve a large distributed brain network. How valence is transformed from sensory signals however is unknown. As structures outside the traditionally recognized limbic system and related circuitry have not been well studied under the context of reward/punishment, it remains possible that even at an early sensory information processing stage preceding the classic limbic system, valence information has already been processed by specific neuronal populations.

In humans, previous studies have suggested that the pons could work conjunctively with the distributed corticolimbic system to shape an individual's affective states [31,32], especially for negative affective states [33]. In particular, the dorsal pons has been found activated during recalled experiences of negative emotion [34]. These findings raise a possibility that specific structures in the dorsal pons might be involved in valence and emotional processing. Here, we directly targeted a salient structure located in the dorsal pons, the pontine central gray (PCG). The PCG is a distinct cell group in caudoventral regions of the pontine periventricular gray, adjacent to the caudal dorsal tegmental nucleus (DTN). Previous studies in related areas have mostly been focused on sleep-wake regulation [35,36], as well as sensory relay [37-40]. The anatomical and functional roles of PCG in valence processing remain largely unclear.

By combining *in vivo* electrophysiology and fiber photometry recording, we found that two genetically defined neuronal populations in PCG encoded opposite valences. The glutamatergic neurons were specifically activated by aversive but not reward sensory inputs, while the GABAergic neurons responded preferentially to reward signals. Optogenetic activation of the glutamatergic and GABAergic neurons acutely resulted in avoidance and preference behaviors, respectively, and was sufficient to induce conditioned place aversion (CPA) or preference (CPP). On the other hand, optogenetic suppression of these neurons attenuated sensory-induced aversion and reward-related behaviors. Using cell-type-specific anatomical tracing and projection-specific manipulations, we found that the two PCG neuronal populations had largely overlapping yet distinguishable input-output patterns. They receive the most prominent input from the pontine reticular nucleus (PRN) and orbital frontal cortex (OFC), respectively. Through distinct output projections, they relay the valance-specific information into a distributed brain network known to be involved in motivational processing. Our results suggest that PCG, while at a relatively early stage of sensory processing, can already distinguish sensory valences through the activity of two functionally opponent neuronal populations. Together, we conclude that PCG plays an important role in valence processing and serves as a critical hub to broadcast valence-specific signals globally to a distributed brain system.

Results

PCG mediates sensory-induced aversion and reward-related behaviors

We examined the affective behavioral effect of various sensory cues and the involvement of PCG by infusing muscimol to silence PCG (Figure 1A, Figure S1A). We first exploited a two-chamber place preference test [38,41,42] (see Methods). Loud noise sound (80 dB

sound pressure level [SPL]) or wind blow was applied whenever a naïve mouse entered the predesignated “stimulation” chamber (Figure 1B, Figure S1B). These aversive sensory stimuli greatly reduced the time spent by the animal in that chamber compared to control conditions without sensory stimulation (Figure 1B and 1C, Figure S1B and S1C), confirming the innately aversive nature of the auditory and somatosensory stimulation [38]. Moreover, the average speed of movements was much higher in the stimulation than non-stimulation chamber (Figure 1D), demonstrating that the animal rapidly escaped from the stimulation to the non-stimulation chamber. Silencing PCG activity significantly reduced this avoidance behavior and the locomotion increase induced by the aversive sensory stimuli, whereas saline infusion had no effects (Figure 1C and 1D, Figure S1C and S1D). These results indicate that PCG plays a role in mediating sensory-induced aversion.

To examine whether PCG also plays a role in reward-related behavior, we adapted a sucrose preference test [43,44] (see Methods). In this test, water-deprived mice could choose to lick from one of two bottles to acquire liquid of 2% sucrose or just water (Figure 1E). Muscimol inhibition of PCG activity resulted in a significant reduction of relative sucrose intake compared to the pre-injection condition, whereas saline had no effect (Figure 1F). This indicates that activity of PCG also plays a role in mediating appetitive behavior.

Both aversive and rewarding stimuli can elicit arousal [11,45]. To study arousal induced by salient events, we measured the pupillary change in awake head-fixed animals responding to aversive (70 dB SPL noise and air puffs) and rewarding (sucrose water) stimuli (Figure 1G). Pupillary responses are known to reflect arousal state [46-48]. Both the aversive and appetitive sensory stimuli induced a large increase in pupil size in naïve mice (Figure 1H and 1I), consistent with the notion that both positive and negative valence events can induce arousal [49-51]. Muscimol silencing of PCG activity significantly attenuated the arousal effect (Figure 1J and 1K), whereas saline had no effect (Figure S1E). Thus, PCG also plays a role in mediating arousal elicited by salient stimuli.

By applying fluorescence *in situ* hybridization with RNA probes (RNAscope) for vesicular glutamate transporter 2 (Vglut2) and vesicular GABA transporter (Vgat), we estimated the relative abundance and spatial distribution of glutamatergic and GABAergic neurons in PCG (Figure 1L). About 60% and 40% of neurons in PCG were found to be glutamatergic (i.e. Vglut2+) and GABAergic (Vgat+), respectively (Figure 1M). However, in its neighboring structure, DTN, GABAergic neurons predominated over glutamatergic neurons (Figure 1M).

PCG Glutamate and GABA neurons drive opposing valence-specific behaviors

As glutamatergic neurons were a slightly more dominant cell type in PCG, we tested the behavioral effect of optogenetic activation of these neurons by injecting adeno-associated virus (AAV) encoding Cre-dependent Channelrhodopsin-2 (ChR2) fused with enhanced yellow fluorescent protein (eYFP) (or eYFP alone as control) in Vglut2-Cre mice (Figure 2A, Figure S2A). To assess the valence effect of the photo-activation, we employed an optogenetics-coupled real-time place preference (RTPP) test following previous studies [38,42]. In the test, whenever the mouse entered the designated stimulation (LED-On) chamber, LED pulses (470 nm, 5-ms duration, at 20 Hz) were continuously delivered through bilaterally implanted optic fibers above PCG until it exited. We found that ChR2-expressing

mice spent significantly less time in the LED-On chamber than the eYFP control mice, with the latter spending about equal amounts of time in LED-On and LED-Off chambers (Figure 2B and 2C). Lower stimulation frequencies generated weaker effects (Figure S3A). The photo activation also greatly suppressed food intake in hungry mice (food deprived for 24 hours) (Figure S3B). These results suggest that PCG glutamatergic neurons drive negative-valence specific behaviors. In addition, it acutely increased locomotion in an open field (Figure 2D and 2E).

Next, we tested the effect of photostimulation of PCG GABAergic neurons by injecting Cre-dependent ChR2 virus in Vgat-Cre mice (Figure 2F). Opposite to that of the glutamatergic neurons, activation of the GABAergic neurons led to a strong preference for the LED-On chamber in the RTPP test (Figure 2G and 2H). This indicates a rewarding effect of these neurons, although no effect on locomotion was observed (Figure 2I and 2J). Thus, our data demonstrate that activity of PCG glutamatergic and GABAergic populations drives negative and positive valence-specific behaviors, respectively.

Furthermore, we tested whether the acute valence effects of PCG neurons could support CPA or CPP [52,53]. To this end, we employed a four-day test-conditioning-test strategy (Figure 2K) by selectively pairing optogenetic stimulation (20 Hz, 20 min) with one designated chamber over day 2-3. On day 4 (testing day), ChR2-expressing Vglut2-Cre animals exhibited avoidance from the paired LED-On chamber although no LED light was applied, while before conditioning (day 1) they did not show preference for either chamber (Figure 2L). This result indicates that photo-activation of the PCG glutamatergic neurons had enabled CPA. On the contrary, photo-activation of PCG GABAergic neurons resulted in CPP (Figure 2M). Thus, our results further indicate that activities of PCG glutamatergic and GABAergic populations are associated with negative and positive valence, respectively.

Consistent with the affective effects, we found that activation of both PCG glutamatergic and GABAergic neurons led to enhanced arousal, as shown by the robust pupil dilation after the onset of light activation (20 Hz, duration 3-s), which was absent in the eYFP control mice (Figure 2N-2Q). Together, our results demonstrate opposing valence effects of activating PCG glutamatergic and GABAergic neurons, with both strongly enhancing arousal.

PCG glutamate and GABA neurons respond to aversive and rewarding sensory events respectively

Since PCG glutamatergic and GABAergic neurons drive negative and positive valence effects, respectively, we wondered whether they could be activated by aversive and rewarding sensory events, respectively. To test this, we performed optrode recording from photo-tagged neurons by injecting AAV-DIO-ChR2 into PCG of Vglut2-Cre/Vgat-Cre animals. Recording was performed in the awake head-fixed mouse, following our previous studies [10,38]. Of 298 units recorded in Vglut2-Cre mice, 121 neurons were identified as Vglut2+ neurons, as demonstrated by their time-locked spike responses (latency < 3 ms) to applied blue light pulses (Figure 3A). As shown by an example ChR2-tagged glutamatergic neuron (Figure 3B) and the population response (Figure 3D), the majority of PCG Vglut2+ neurons (79/121) were excited by an aversive event (loud noise or air puffs) (Figure 3E, 3L). Most of them (60/79) were responsive to both the auditory and somatosensory stimuli

(Figure 3E). For the remaining 177 untagged units, which presumably contained mainly GABAergic neurons, only 15.8% (28/177) responded to either noise or air puffs stimulation while the great majority were unresponsive (Figure 3E). Consistent with this data, in our recorded photo-tagged GABAergic neurons from Vgat-Cre mice (63 out of 112 units), only 9.5% (6/63) showed excitatory responses to the aversive auditory or somatosensory stimulation (Figure 3H, 3I, 3L), while in the untagged population from Vgat-Cre mice 69.3% (34/49) (presumably glutamatergic neurons) did so (Figure 3I).

We then tested whether the GABAergic neurons could respond to rewarding sensory signals by delivering sucrose solution (5% w/v, 10 μL per trial) into the oral cavity of water-deprived mice via intraoral cheek fistulae (see Methods). In photo-tagged GABAergic neurons (an example is shown in Figure 3C), the majority of them (72.2%, 39/54 units) showed increases of firing rate following the sucrose delivery (Figure 3J, 3K, 3M), while 22.2% of the population (12/54) showed no change and 5.6% (3/54) showed a decrease in firing rate (Figure 3K). In the untagged population, only 6.2% (5/80) showed an excitatory response to sucrose and the great majority showed no response (93.8%, 75/80) (Figure 3K). Consistent with this data, only 8.1% (3/37) of photo-tagged Vglut2+ neurons showed excitatory responses to sucrose, while in the untagged population 68% (34/50) did so (Figure 3F and 3G). The glutamatergic and GABAergic neurons did not differ in spontaneous firing rate (3.1 ± 1.8 Hz vs. 3.4 ± 1.6 Hz, n = 121 and 63 neurons, P = 0.29, *t*-test).

We also applied fiber photometry [54,55], recording of the ensemble Ca^{2+} signal in PCG of freely moving mice (Figure 3N, Figure 3Q) by injecting AAV expressing Cre-dependent Ca^{2+} indicator (AAV1-DIO-GCaMP6s) into Vglut2-Cre/Vgat-Cre mice [56]. Consistent with the single-unit data, the Vglut2+ population showed increases of Ca^{2+} activity in response to noise, air puffs as well as to foot shocks (Figure 3O and 3P). In contrast, activity of the Vglut2+ population was essentially not affected by sucrose delivery (Figure 3O and 3P). On the other hand, the Vgat+ population in water-deprived mice was preferentially activated by sucrose water, but not by noise, air puffs or foot shocks (Figure 3R and 3S). Together, our results strongly suggest that PCG glutamatergic neurons are selectively activated by a range of aversive sensory stimuli across modalities while its GABAergic population is preferentially activated by rewarding sensory signals.

Suppression of PCG glutamate and GABA neurons attenuates sensory-induced aversion and appetitive behavior respectively

Since PCG glutamatergic neurons drives negative valence and can be activated by aversive sensory stimuli, we wondered whether suppressing the activity of these neurons could specifically impair aversive sensory-induced behaviors. We inhibited these neurons by injecting AAV expressing Cre-dependent ArchT in Vglut2-Cre and applying green LED light (Figure 4A). The photo-inhibition of the Vglut2+ neurons alone did not induce any place preference/avoidance or any change in pupil size (Figure S4A-S4E), suggesting that the baseline activity of these neurons might not significantly affect the affective state. However, the optogenetic inhibition greatly reduced the avoidance behavior (Figure 4B and 4C), locomotion increase (Figure 4D) and pupil dilation (Figure 4E and 4F, Figure S5A and S5B) induced by aversive sensory stimulation, without generating a significant effect on

reward-related behavior (Figure S5C and S5D). Thus, our data suggest that sensory-evoked activity of PCG glutamatergic neurons is specifically required for aversive sensory-induced behavior.

We further tested the involvement of PCG GABAergic neurons in reward-related behavior, by injecting AAV expressing Cre-dependent ArchT in Vgat-Cre mice (Figure 4G). Optogenetic inhibition of the Vgat+ neurons alone did not produce any valence effect or changes in pupil size (Figure S4F-S4J). In the sucrose preference test, we compared LED-on vs. LED-off epochs. The photo-inhibition resulted in a significant reduction of sucrose intake in the ArchT-expressing group, whereas no effect was observed in GFP control mice (Figure 4H). It also greatly reduced the pupil dilation induced by rewarding sucrose stimulation (Figure 4I and 4J). On the other hand, the optogenetic inhibition of the Vgat+ neurons had no effect on the avoidance behavior (Figure S5E and S5F), locomotion increase (Figure S5G) or pupil dilation (Figure S5H and S5I) induced by aversive sensory stimulation. These data suggest that sensory-evoked activity of PCG GABAergic neurons is specifically required for sensory-induced appetitive behavior.

PCG glutamate and GABA neurons share similar projection patterns

Since the activation of PCG glutamatergic and GABAergic neurons produced very different behavioral outcomes, we wondered whether they projected to different downstream targets. To address this question, we injected AAV-FLEX-GFP into PCG of Vglut2-Cre or Vgat-Cre mice (Figure 5A, 5C). To our surprise, GFP-labeled glutamatergic and GABAergic PCG axons exhibited similar projection patterns (Figure 5B, 5D), mainly on the ipsilateral side (Figure 5E and 5F). Among the diverse brain regions targeted by PCG, structures such as the mediodorsal nucleus of the thalamus (MD), paraventricular thalamus (PVT), lateral hypothalamic areas (LHA), ventral tegmental area (VTA), lateral preoptic area (LPO) and medial septum-diagonal band nucleus (MS/DB) were strongly innervated by both the glutamatergic and GABAergic axons (Figure 5E and 5F). Most of these structures have been implicated in motivated behaviors [6,7,10,38,52,57,58]. Therefore, PCG glutamatergic and GABAergic neurons both feed valenced sensory information into a large network which is highly engaged in processing emotionally salient information.

We furthered explored intra-PCG connectivity by specifically expressing ChR2 in PCG GABAergic neurons in Vgat-Cre::Ai14 mice. In slice preparations, we performed whole-cell recording selectively from PCG glutamatergic neurons (tdTomato-) in the presence of TTX and 4AP while optically stimulating PCG GABAergic neurons (Figure S6). Light-evoked monosynaptic inhibitory postsynaptic currents (IPSCs) were observed in the glutamatergic neurons, indicating that the GABAergic neurons can suppress local glutamatergic neurons. This local inhibition suggests a competitive interaction between the pathways mediated by the two PCG cell types, which may contribute to their opposing valence effects.

PCG mediates aversion and reward behaviors through distinct downstream targets

To further examine which of the downstream projections mediates the PCG-dependent behavioral effects, we optically activated ChR2-expressing axonal terminals from PCG glutamatergic (Figure 6A) or GABAergic neurons (Figure 6G) in each of the aforementioned

target areas and at the same time silenced PCG cell bodies with muscimol to prevent the potential spread of antidromic spikes to undesired targets. Bilateral stimulation of PCG glutamatergic axons in the MD, VTA, LHA and MS/DB resulted in avoidance behavior (Figure 6B and 6C) and enhanced arousal (Figure 6E and 6F). In addition, the stimulation of PCG-to-MD, PCG-to-LHA and PCG-to-MS/DB axons significantly increased locomotion speed (Figure 6D). However, stimulation of the PCG projections to PVT and LPO in general had no obvious effect on aversion (Figure 6C), arousal (Figure 6F) or locomotion speed (Figure 6D), except that stimulation of the PCG-to-LPO projection produced weak aversion (Figure 6C). Different from the glutamatergic projections, stimulation of the PCG GABAergic projections VTA, LHA and MS/DB (but not MD) resulted in place preference (Figure 6H and 6I) and enhanced arousal (Figure 6K and 6L). Stimulation of the GABAergic projections to LPO, PVT and MD did not produce significant behavioral effects (Figure 6I and 6J, 6L), and none of the GABAergic projections tested had an effect on locomotion (Figure 6J). Together, these data suggest that PCG glutamatergic and GABAergic neurons may mediate aversion and reward-related behaviors through overlapping yet distinguishable downstream targets.

We further tested the involvement of specific PCG projections in sensory-induced aversion or reward-related behavior by optogenetically inhibiting PCG glutamatergic/GABAergic axons in two selected targets, VTA and LHA (Figure 7A, 7E, 7I), after injecting AAV encoding Cre-dependent halorhodopsin (eNpHR3.0). Inhibiting the glutamatergic axon terminals in both VTA and LHA significantly attenuated the avoidance behavior (Figure 7B, 7F) and pupil dilation (Figure 7D and 7H, Figure S7A and S7B, S7D and S7E) induced by aversive but not rewarding sensory stimulation (Figure S7C and S7F). In addition, inhibiting the glutamatergic axon terminals in LHA (Figure 7G) but not VTA (Figure 7C) reduced the locomotion effect. On the other hand, inhibiting the GABAergic projections to both VTA and LHA resulted in a reduction of sucrose intake (Figure 7J, 7L). It also attenuated the pupil dilation induced by rewarding sucrose stimulation (Figure 7K, 7M) but not that induced by aversive sensory stimulation (Figure S7G-S7L). These results confirm that PCG relays valence-specific signals to multiple targets to mediate sensory-induced aversion and reward-related behaviors.

Overlapping but distinguishable inputs to PCG glutamate and GABA neurons

Finally, we sought to identify monosynaptic inputs to PCG glutamatergic and GABAergic neurons by applying cell-type-specific retrograde tracing with pseudotyped glycoprotein-deficient rabies virus [59-61] (Figure 8A, 8E). We found that although the glutamatergic and GABAergic neurons shared some common input sources, the strongest input sources were clearly different between these two populations. The excitatory neurons received the strongest input from the PRN (Figure 8C and 8D), while the inhibitory neurons from the OFC (Figure 8G and 8H), which has been shown to be involved in regulating emotional and reward-related behaviors [62-65]. Thus, PCG glutamatergic and GABAergic neurons receive distinguishable inputs, possibly conferred by their differential roles in valence processing.

Discussion

In this study, with cell-type specific approaches, our data have elucidated a circuit mediated by PCG (Figure S8C) to relay valence-specific sensory information into an extended valence processing network. Our results showed that PCG glutamatergic and GABAergic neurons play opposing functional roles: the glutamatergic neurons are activated by aversive sensory stimuli and drive avoidance behavior, while the GABAergic neurons are activated by rewarding stimuli and drive appetitive behavior. In addition, the activity of these two cell populations is sufficient for the formation of association of initially neutral sensory cues with reward/aversion. Our results suggest that PCG may serve as a critical node in bottom-up sensory pathways to process valence-specific information of incoming sensory signals and mediate appropriate behavioral responses.

PCG encodes opposite valences via two distinct neuronal populations

Our previous studies have suggested that PCG can provide sensory input to the medial septum [37] and that the glutamatergic projection from the medial septum to the lateral habenula can account at least partially for the avoidance behavior induced by aversive sound stimuli [38]. However, whether PCG itself is also involved in valence processing is unclear and functional roles of PCG beyond a simple sensory relay remain poorly understood. In the present study, we demonstrated that in PCG, a sensory information processing stage preceding the classic limbic system, valence processing already occurs. Conforming to the definition of valence coding neurons [3,11,27,55], PCG neurons have differential responses to aversive and reward sensory stimuli: the glutamatergic neurons are selectively activated by aversive cues across multiple sensory modalities while the GABAergic neurons are preferentially activated by reward cues. The behavioral outcomes of the activation of these neuronal populations are also negative and positive valence specific, avoidance and preference, respectively. Consistent with the notion that both reward and punishment can induce emotional arousal [11,66], activation of both cell types leads to elevated arousal levels. In addition, the ability of inducing CPA or CPP by activating PCG neurons alone further supports that PCG activity is not simply for sensory relay but contains valence-specific information. Thus, our results have revealed a previously unrecognized functional role of PCG in valence processing. Through two separate neuronal populations, PCG can encode both negative and positive valences and mediate valence-specific motivational behaviors. Interestingly, the co-existence of negative valence representing glutamatergic neurons and positive valence representing GABAergic neurons in the same structure is also found in several other brain areas including the ventral pallidum [67,68], medial septum [10,38], bed nucleus of the stria terminalis (BST) [69], LHA [6,7] and medial preoptic area (MPO) [55]. This suggests that coding of opposite valences by neuronal populations defined by inherently opponent neurotransmitter types may be a general strategy employed in the mammalian nervous system.

Broad integration of information by PCG

The anatomical connections of different cell types in PCG, to our knowledge, have not been characterized previously [70]. The cell-type specific monosynaptic retrograde tracing results indicate that the PCG glutamatergic and GABAergic neurons receive inputs from broad,

partially overlapping sources (Figure 8), including midbrain, thalamic, hypothalamic, basal forebrain and cortical regions. The profiles of strengths of their diverse inputs are clearly different. The most prominent input to the glutamatergic neurons arises from the PRN, which is a multisensory nucleus [71]. The PRN is thought as a sensorimotor interface [72] and multisensory information can be relayed via PRN to other brain structures. Thus, it is likely that PCG glutamatergic neurons receive bottom-up multisensory input from the PRN, which sits at a lower-level in the hierarchy based on the onset latency of responses to aversive sound stimuli [37].

Although PCG GABAergic neurons also receive bottom-up input from the PRN, their most prominent input is interestingly from the OFC (Figure 8), which has been shown to be involved in processing reward value, mood and emotion [64,73]. Such circuit design may conform to the nature of reward cues. While there are many innately aversive sensory stimuli, innately rewarding cues are few and often the assignment of positive valence strongly depends on the context, prior experience, or internal states of the animal [12,74]. Likely, the assignment of positive valence has to be strongly modulated by top-down input, e.g. orbital frontal cortical input that represents appraisals of surroundings or information about prior knowledge. In addition, OFC has been shown to encode high-level cognitive signals [65,75]. By exerting influence on valence-specific expression of motivational behavior via its projection to PCG, OFC can then play a role in cognitive regulation of emotion. Considering the prominent top-down inputs from the frontal cortex to its GABAergic neurons, PCG may not simply serve as an important node in bottom-up sensory pathways, but can also play other roles in emotional behaviors.

It is worth noting that PCG also receives input from the interpeduncular nucleus (IPN), which is involved in addiction, anxiety, and mood regulation [76,77]. In addition, it receives moderate excitatory input from the lateral habenula, a structure involved in processing of aversive information and mood [78], as well as from other regions known to be involved in valence processing such as VTA and LHA [7,14,79]. Taken together, the broad inputs (including both bottom-up and top-down) to both the PCG glutamatergic and GABAergic neurons suggest that their valence coding properties may be modulated by a multitude of factors and their activity may be modulated at different timescales depending upon the source of input.

PCG broadcasts valence-specific information to an extended brain network

Our anterograde tracing results indicate that axons from the PCG may be divided into two ascending streams (dorsal and ventral streams, see Figure S8C) that innervate various targets in the midbrain, thalamus, hypothalamus and basal forebrain. Outputs of its glutamatergic and GABAergic neurons are directed to essentially the same targets, including MD, LHA, VTA, MS/DB, LPO, MPO, medial mammillary nucleus (MM), midbrain reticular nucleus (MRN), superior central nucleus raphe (CS) and periaqueductal gray (PAG). PCG neurons, especially the glutamatergic population, send dense projections to MD, which is known to form reciprocal interactions with the prefrontal cortex and play a critical role in complex cognitive behaviors and decision making [80,81]. PCG also innervates MS/DB, SuM and MM, which are involved in regulating hippocampal related functions including memory

processing, spatial learning, navigation and theta oscillations [82-84]. We also found obvious projections in the MRN and CS. The former is involved in locomotion [85] and the latter plays a pivotal role in regulating mood, fear, and anxiety [86,87] as well as memory consolidation [88]. Therefore, it is likely that PCG activity can engage a large extended brain network and that it serves as an important hub to control a set of functions even beyond valence processing.

Despite the apparent overlap of anatomical targets, our behavioral tests of PCG projections to a set of selected targets indicated that the valence effects of PCG glutamatergic and GABAergic populations are mediated through distinguishable downstream effectors. The negative valence effect of PCG is achieved mainly through its glutamatergic projections to MD, VTA, LHA, MS/DB and LPO (Figure S8C). The positive effect is through its GABAergic projections to VTA, LHA and MS/DB (Figure S8C). Due to the large overlap of these targets, the local suppressive effect within PCG (Figure S6) can serve as a simple mechanism for producing opposite valence effects by the two PCG cell types, while the difference may reflect a difference in how negative and positive valence information is processed downstream of PCG. While the aforementioned structures have all been shown to be associated with emotional processing in numerous studies [10,14,38,79,89-92], particular attention is drawn to the VTA and LHA. Specifically, activation of VTA dopaminergic neurons causes place preference [52], and suppression of VTA dopaminergic neurons by activating VTA GABAergic neurons leads to place aversion [57]. Activation of LHA GABAergic neurons promotes feeding and reward phenotypes [6], while that of LHA glutamatergic neurons suppresses feeding and produces aversive behavioral phenotypes [7]. Based on these previous findings, we hypothesize that PCG glutamatergic and GABAergic axons can converge onto single VTA GABAergic neurons in a circuit configuration analogous to a so-called “opposing components” motif [3]. By opposingly regulating the activity of VTA dopaminergic glutamatergic neurons indirectly through the local GABAergic cells, they would be able to generate opposite behavioral effects: avoidance and preference, respectively. In our additional slice whole-cell recording experiment, we confirmed that individual VTA GABAergic neurons could receive both excitatory and inhibitory inputs from PCG (Figure S8A and S8B). Alternatively, via a “labeled lines” motif [3], the PCG glutamatergic and GABAergic neurons may relay the negative and positive valence information in parallel to the next-stage glutamatergic and GABAergic neurons, respectively, e.g. in LHA and MS/DB, from where the valence information is further processed. It will be of great interest to further verify these hypothetical circuits in the PCG target structures in future studies. Interestingly, our results showed that activation of PCG to PVT axons did not produce any obvious valence effect. This observation may be consistent with a recent study showing that PVT neurons encode stimulus salience irrespective of valence [93].

In summary, our results reveal an important role of PCG in valence processing. Importantly, we show that both excitatory and inhibitory PCG neurons can drive motivated behavior, with opposite valences. By broadly receiving multisensory inputs of both aversive and rewarding nature, PCG processes and then broadcasts positive and negative valence information of sensory cues to an extended network critically involved in emotional/motivational processing.

STAR★METHODS

RESOURCE AVAILABILITY

Lead contact—Further information and requests for resources and reagents should be directed to and will be fulfilled by the Lead Contact, Li I. Zhang (liizhang@usc.edu).

Materials availability—This study did not generate new unique reagents.

Data and code availability

- All data reported in this paper will be shared by the lead contact upon request.
- All original code has been deposited at Zenodo and is publicly available as of the date of publication. DOIs are listed in the key resources table.
- Any additional information required to reanalyze the data reported in this paper is available upon request.

EXPERIMENTAL MODELS AND SUBJECT DETAILS

All experimental procedures in this study were in accordance with the guidelines for the care and use of laboratory animals of the US National Institutes of Health (NIH), and were approved by Animal Care and Use Committee (IACUC) of the University of Southern California. Experiments were performed in adult (2–4 months old) male and female mice. The Vglut2-ires-Cre (stock # 016963), Vgat-ires-Cre (stock # 016962), Ai14 (Cre-dependent tdTomato reporter line; stock # 007914) and C57BL/6J (stock # 000664) mice were obtained from the Jackson Laboratory and were housed with a 12 h light-dark cycle, at 18–23°C temperature and 40–60% humidity. All recordings and behavioral tests were conducted in the dark cycle.

METHOD DETAILS

Abbreviation of mouse brain structures—All mouse brain structures in this study are referenced to the Allen Brain Atlases (https://atlas.brain-map.org). ARH, arcuate hypothalamic nucleus; BST, bed nuclei of the stria terminalis; CNU, cerebral nuclei; CTX, cerebral cortex; CB, cerebellum; CUN, cuneiform nucleus; CS, superior central nucleus raphe; DMH, dorsomedial nucleus of the hypothalamus; DR, dorsal nucleus raphe; DTN, dorsal tegmental nucleus; DB, diagonal band nucleus; fr, fasciculus retroflexus; HPF, hippocampal formation; HY, hypothalamus; IMD, intermediodorsal nucleus of the thalamus; IPN, interpeduncular nucleus; IF, interfascicular nucleus raphe; ICe, external cortex of the inferior colliculus; LH, lateral habenula; LS, lateral septal nucleus; LPO, lateral preoptic area; LHA, lateral hypothalamic area; MOB, main olfactory bulb; MB, midbrain; MY, medulla; MH, medial habenula; MD, mediodorsal nucleus of the thalamus; MS/DB, medial septum and diagonal band nucleus; MPN, medial preoptic nucleus; MOs, second motor area; MA, magnocellular nucleus; MPO, medial preoptic area; MM, medial mammillary nucleus; OFC, orbitofrontal cortex; OT, olfactory tubercle; PVT, paraventricular nucleus of the thalamus; PAG, periaqueductal gray; PG, pontine gray; PCG, pontine central gray; PRN, pontine reticular nucleus; PL, prelimbic area; P, pons; RSP, retrosplenial cortex; SOC, superior olivary complex; SC, superior colliculus; SI, substantia innominate; SuM,

supramammillary nucleus; SNr, substantia nigra reticular part; TH, thalamus; VTA, ventral tegmental area; VMH, ventromedial hypothalamic nucleus; VM, ventral medial nucleus of the thalamus; ZI, zona incerta.

Viral Injection—AAV1-CAG-FLEX-GFP-WPRE (Addgene, 51502), AAV1-EF1α-DIO-hChR2 (H134R)-EYFP-WPRE (Addgene, 20298), AAV1-Ef1a-DIO-eNpHR 3.0-EYFP (Addgene, 26966), AAV1-hSyn-hChR2 (H134R)-EYFP (Addgene, 26973), AAV1-EF1a-DIO-eYFP-WPRE (Addgene, 27056), AAV1-CAG-FLEX-ArchT-GFP (Addgene, 29777), AAV1-Syn-FLEX-GCaMP6s-WPRE-SV4 (Addgene, 100845), AAV1-Syn-FLEX-TVA-EGFP-tTA (Addgene, 100798), AAV1-TREtight-mTagBFP2-B19G (Addgene, 100799) [59,60], RVΔG-4mCherry (EnvA) [61] were used in this study. Stereotaxic injection of viruses was conducted as we previously described [99-101]. Mice were placed on a heating pad and were anesthetized with 1.5% isoflurane (in oxygen) by inhalation during the whole surgery procedure. Buprenorphine was injected subcutaneously after anesthesia. After asepsis, a small incision was made on the skin and the muscles were slightly removed to expose the skull. For virus injection, a 0.2 mm craniotomy window was made for the target region (PCG, AP −5.5 mm, ML +0.4 mm, DV −3.2 mm). Stereotaxic coordinates of injection were based on the Allen Reference Atlas www.brain-map.org. For pressure injection, the virus was delivered through a pulled glass micropipette with beveled tip (~20 μm diameter) via a micropump (World Precision Instruments). The volume for each injection was 50 nl and injected at a rate of 15 nl/min. For iontophoresis injection, 3 μA current was applied (7 sec on, 7 sec off cycle) for 5 min. The pipette was allowed to rest at the injection site for 5 min before being withdrawn slowly. The scalp was then sutured. After the surgery, antibiotic ointment was applied to the surgery wound before returning the animals to their home cages. Ketoprofen (0.5 mg/kg) was applied for three days following all the surgeries. Viruses were expressed for at least 3 weeks before behavioral, tracing or recording experiments. After each experiment, the brain was sectioned and automatically imaged under a confocal microscope to confirm viral expression. To trace the monosynaptic input to Vglut2+ or Vgat+ neurons in PCG, AAV1-Syn-FLEX-TVA-EGFP-tTA and AAV1-TREtight-mTagBFP2-B19G were mixed (1:1) and stereotactically injected into PCG of Vglut2-Cre or Vgat-Cre mice, after one week, RVΔG-4mCherry (EnvA) was injected at the same site.

Optogenetic Manipulation—For optogenetic manipulations, optical fibers were implanted into the targeted region two weeks after the virus injection (PCG, bilateral implantation, AP −5.5 mm, ML +1.75 mm, DV −3.1 mm, with a 15° angle; MD, bilateral implantation, AP −1.2 mm, ML +1.5 mm, DV −3.0 mm, with a 15° angle; PVT, unilateral implantation, AP −1.2 mm, ML +0.6 mm, DV −2.7 mm; with a 10° angle; LHA, bilateral implantation, AP −1.5 mm, ML +1.2 mm, DV −4.7 mm, with a 10° angle; LPO, bilateral implantation, AP +0.2 mm, ML +1.2 mm, DV −4.5 mm, with a 10° angle; VTA, AP −3.2 mm, ML +1.5mm, DV −4.3 mm, with 11° angle; MS, unilateral implantation, AP + 0.85 mm, ML +0.5 mm, DV −3.6 mm, with a 10° angle;). Animals were anesthetized with 1.5% isoflurane and a small hole was drilled. The optic cannulas (200 μm core, NA=0.22, RWD Inc.) were lowered into the targeted depth and was fixed with dental cement. A metal screw for head fixation was mounted on the top of the skull for animal pupil size

tests. After surgery, the animals were allowed to recover for at least 3 days before the experiments. Before any behavioral tests, mice were connected to optical cables without LED stimulation for habituation for three days. To block the light leak, a black tape wrapped around the connection between optical cable and implanted ferrule. For all the optogenetic activation experiments, the blue LED source (470 nm, 20 Hz, 5-ms duration, Thorlabs) was used. For the optogenetic silencing experiments, the green (530 nm, Thorlabs) or yellow light (589 nm, Thorlabs) was delivered continuously. All light was delivered at about 7–10 mW (measured from the fiber tip). For noise or air puff-induced place aversion test combined with optogenetic inhibition, green LED light and 80 dB SPL noise or air puff were delivered simultaneously. For stimulation of PCG projections in different target regions, 100 nL muscimol (0.7 mM in ACSF with 5% DMSO) was applied to the PCG via a pipette connected to a microinjector before behavioral tests to silence PCG neurons. All the control groups received the same experiment procedures and light stimulation. After each experiment, animals were transcardially perfused and examined the location of the viral expression and the track of optical fibers.

Awake Head-Fixed Animal Preparation—For awake recording from head-fixed animal preparations, the procedures were similar as previously described [37,102-105]. Mice were placed on a heating pad and anesthetized with 1.5% isoflurane, and a screw for head fixation was mounted on top of the skull with dental cement. One day before the recording, a craniotomy window was made over the recording region (PCG: AP −5.4 – −5.7 mm, ML +0.4 mm, DV −3.1 – −3.5 mm). Silicone adhesive (Kwik-Cast Sealant, WPI Inc.) was applied to cover the craniotomy window until the recording sessions. Animals were allowed to recover for one week before all the recording experiments. Mice were trained to run freely on a rotatable plate during the recovery period.

Sound Generation—The sound stimulation and data acquisition were generated by custom-written software in LabVIEW (PCI-6731 NI board for sound generation, 16-bits output, 1MHz sampling rate, National Instruments, Austin, TX). For in vivo head-fixed recording, broadband white noise (100-ms duration, 50 trials, with-5-s inter-stimulus interval) at 70 dB SPL were applied. An open field speaker (MF1, Tucker-Davis Technologies) was placed to the contralateral side and 10 cm away from the ear. For noise-induced pupil dilation test, 70 dB SPL white noise (3-s duration, 30 trials, 30-s inter-stimulus interval) were used. For noise-induced place aversion test, 80 dB SPL white noise was continuously delivered through a speaker which was placed in a corner of the designated stimulation chamber whenever the mouse entered that chamber.

Air Puff Stimulation—The air puffs were generated by the center air with an internal pressure of around 40-55 psi. A microvalve (LFAA1209512H, Lee Co, ESSEX, CT) was used to deliver and control the intensity of the air puff. For in vivo awake mice recoding, air puffs were delivered to the back of the mouse with minimum waiting intervals of 60 s. For air puff induced place aversion, a battery powered fan was used to deliver the continuous wind blow in the designated stimulation chamber. For air puff induced pupil size change, we followed previous methods [50,106], a small tube was positioned behind the mice's back and

air puffs (3-s duration, 30 trials, with 60 s inter-stimulus interval) were delivered to the body of the mouse in the head-fixed mice.

Pharmacological silencing—For pharmacological silencing of PCG, mice underwent a drug cannula implantation surgery one week before the pharmacological manipulation. Surgery procedure was similar to optical fiber implantation as described above. Mice were anesthetized with isoflurane and a drug cannula (internal diameter: 140 μm) was implanted bilaterally into the PCG. Fluorescent muscimol-bodipy (0.7 mM in ACSF with 5% DMSO) or saline was infused via the implanted cannula ten minutes before behavioral tests. A thin pipette connected with a microinjector for drug injection was inserted through the implanted drug cannula, and muscimol (100 nL, per hemisphere) was slowly perfused into the PCG bilaterally. The mouse was perfused transcardially to examine the location of cannula and drug spread after the experiments.

Optrode Recording—All the in vivo recordings were performed in a sound-attenuation room (Acoustic Systems) as previously described [37,38]. Silicon seal was removed, then a 16-channel silicon probe (NeuroNexus Technologies) was lowered into the target brain structure. To identify glutamatergic or GABAergic neurons in the PCG, an optrode (A1x16-Poly2-5mm-50 s-177-OA16LP, 16 contacts separated by 50 μm, the distance between the tip of the optic fiber and the probes is 200 μm, NA 0.22, Neuronexus Technologies) connected to a LED light source (470 nm, Thorlabs) via an optic fiber was lowered into the target brain structure. To identify ChR2+ neurons, 16-Hz (5-ms pulse duration, controlled via an Arduino microcontroller) LED pulse trains were delivered intermittently. All signals were recorded and saved for offline analysis. The silicone probe was coated with DiI (Invitrogen) to label the electrode track.

Intraoral Infusion of Sucrose Water—An intraoral cheek fistula surgery was performed following previous studies [54,107]. Briefly, a soft silastic tubing was subcutaneously inserted to the oral cavity of the mouse through a small incision on cheek. The tube was adhesive to the cheek with sutures. This approach allowed us to precisely control the time and volume of sucrose or water delivered into the mouth. For passive sucrose water delivery, the mouse was water deprived for 12 h. After recovery from the surgery, a micro pump (Lee-Company) was used to infuse sucrose water (5% w/v, with 30 s intervals) into the oral cavity through the tube. A custom-written LabVIEW program was used to serve as a trigger signal for each trial.

Fiber Photometry Recording—To obtain calcium signals, 480 nm LED light (Thorlabs) was bandpass filtered (ET470/24M, Chroma), focused by an objective lens (Olympus), and coupled through an optical fiber (O.D.= 400μm, NA = 0.48, 1 m long, Doric) connected to an implanted optic fiber (400μm, NA = 0.5, Thorlabs) via a ceramic sleeve. The LED power was set at 0.02 mW at the tip of the optical fiber. At this power, no significant photobleaching was observed. The fluorescence calcium signal was bandpass filtered (ET525/36M, Chroma) and collected by a photomultiplier tube (H11706-40, Hamamatsu), and then passed through an amplifier (Model SR570, Stanford Research System) and low-pass filtered (30 Hz). Then the current output was converted to a voltage signal by a data

acquisition card (PCI-MIO-16E-4, National Instruments). The photometry voltage signals were digitized at 250 Hz and recorded by LabView software. Data were obtained using custom LabVIEW software and off-line analyzed using custom MATLAB software. No movement-related artifact has been detected in our system.

Behavioral Experiments—All behavior tests were conducted in a sound-attenuation booth (Acoustic Systems) during the dark cycle of the mice. All the behavioral videos were recorded and saved for further offline analysis.

Real-Time Place Preference Test: We carried out the RTPP test following our previous studies [38]. Mouse implanted with optic fibers was placed in a white plastic box (40 cm × 20 cm × 20 cm) with two compartments. The mouse could freely explore between the two compartments through a small opening. For each test session, the mouse was first put into the non-stimulation (randomly assigned) chamber. Whenever the mouse entered the other chamber, 470 nm blue LED (20 Hz, with 5-ms duration) or 530 nm green LED (continuous stimulation) was delivered until the animal exited. The total duration of each session was 20 min. After each session, the chamber was cleaned with 70% alcohol.

Conditioned Place Aversion or Preference Test: A clear acrylic behavior box (50 cm × 25 cm × 25 cm) was divided into three chambers. The three chambers were separated by a corridor and have distinct walls drawings, floor, and shape. The middle chamber has a grey smooth metal plate floor, the left chamber has black and white stripes on the walls and a grid-wire floor, and the right chamber has black and white squares on the walls and a parallel-wire floor. On day 1 (pre-conditioning day), mice freely explored the chambers for 20 min without light. On the 2nd and 3rd day (conditioning days), mice were confined to one of two sides and received either no stimulation or photostimulation (20 Hz, 5 ms pulse duration) for 20-minute periods in the morning and afternoon, respectively. The stimulation chamber was assigned randomly to the animal. On the 4th day (test day), the animal was placed in the middle chamber and could freely get access to all chambers for 20 min.

Pupil Diameter Tracking and Offline Quantification: For pupil monitoring, the mouse head was fixed using a previously implanted head screw and the mouse body was restricted within a rectangle barrel. The mouse eye was illuminated by an infrared LED light source (LIU780A, Thorlabs) and a camera was used to monitor the left or right eye of the mouse and the video of eye images was acquired by Fly Capture2 software. For PCG activation or terminal activation experiments, blue LED (20 Hz, 5-ms pulse duration, 30-trials, with 30-s inter-stimulus interval) was applied bilaterally. For PCG inhibition combined with sensory stimuli, bilateral green LED was applied continuously, and sensory stimulation was presented for 3-s after 2-s of the baseline activity. The total recording duration of each trial was 10-s. The pupil size was analyzed offline with Python 3.4: each frame was Gaussian filtered and the black pupil was extracted using a threshold adjusted for each experiment. A few frames were dropped due to the eye blink and the corresponding pupil size value was estimated using interpolation based on 5 frames before and after the eye blink [55]. For pupil diameter analysis, the baseline was defined as a period of 2-s before LED or sensory stimulation onset. We then calculated the change in pupil size by averaging for a period of 2

to 5-s following the onset of the stimulus, then the peak amplitude of pupil size during the stimulation was calculated and normalized. Trials without LED or sensory stimuli were used as the control to evaluate the spontaneous fluctuations of pupil size.

Open Field Test: Mice were placed in a white plastic test box (60 cm × 60 cm × 30 cm) to test the baseline locomotion activity. They were allowed to move freely to habituate for 5-10 min. Each animal was tested for 1 session per day and each session lasted 16 min, during which blue LED stimulation (20 Hz, duration 60-s, with a 180-s inter-stimulus interval) was applied. The animal's movement track was recorded by an overhead camera.

Food Intake Test: Food intake test was performed in a white plastic box (40 cm × 20 cm × 20 cm) with two compartments. Mice were housed with food and water ad libitum. Before the behavioral test, the animal was food deprived for 24 h with water ad libitum. The mouse was first put into the non-stimulation (randomly assigned) chamber, whenever the mouse entered the other chamber, blue LED stimulation (20 Hz, 5-ms duration) was continuously applied until the animal exited. Standard grain pellets were used as the food sources and put it in the corner of LED-stimulated chamber. The total duration of each session was 20 min. The weight of food consumed was measured after the test block.

Sucrose Preference Test: Mice were first trained for 30 min daily over 5 d to consume either a sucrose solution or only water, from two sipper tubes presented in a custom-built chamber, until they reached a stable preference for sucrose. Animals were water deprived for 24 h before the test and then exposed to one bottle of 2% sucrose water and one bottle of pure water for 1 h. Bottle positions were switched after 30 min. For ArchT-expressing mice, a green LED source (530 nm, constant illumination) were delivered for 1 h. The sucrose preference index was calculated as (sucrose consumption − water consumption) / (sucrose consumption + water consumption).

Foot Shocks: Animals were placed into an acrylic box (25 cm × 25 cm × 30 cm) with metal grid floor. The foot shocks (0.5 mA, 1-s duration) were randomly delivered with inter-trial intervals of 120 s. Shock delivery onset was used as the trigger event for data alignment.

Real-Time Animal Detection and Closed-loop Optogenetic Control—Customized software was used for online real-time animal detection (Python 3.4, http://www.python.org/ with OpenCV library, https://opencv.org/) [108]. The behavior of the animal was monitored using an infrared camera at 24fps. Each frame was gaussian blurred and then binarized. The gravity center for the detected contour was used to determine the location of the animal. In the two-chamber place preference test, the stimulation chamber was randomly assigned (balanced within the group) to each animal. Once the mouse entered the stimulation chamber, a computer-controlled Arduino microcontroller (https://www.arduino.cc/) would generate TTL signals to drive the LED light source (ThorLabs Inc.). The behavior test was run automatically without experimenter's interference and the result was calculated right after each experiment.

RNAscope assay—RNAscope hybridization was performed using the RNAscope Multiplex Fluorescent Reagent Kit v2 Assay (ACD). The assay was performed according

to its manufacturer's instructions. The staining procedures were similar as we previously described [109]. Briefly, wild-type mice were transcardially perfused, and the brains were removed and post-fixed in 4% paraformaldehyde (PFA) for 24 h at 4°C. Then the brain tissue was dehydrated sequentially in 20% and 30% sucrose. Coronal brain sections were cut at 40 μm using a cryostat (CM3050S, Leica). Collected sections were mounted on slides and baked for 30 min at 60°C and post-fixed in 4% PFA for 15 min at 4°C. Then, the sections were dehydrated in increasing ethanol concentrations (50%, 70% and 100%), followed by incubation of Hydrogen Peroxide for 10 min at room temperature (RT). Next, target retrieval was made by immersing the slides into double distilled (dd) H_2O for 10-s and into Retrieval Reagent for 5 min at 99 °C in a humidity saturated environment. The slides were cooled in dd H_2O for 15-s, then transferred to 100% alcohol for 3 min at RT. Then, the sections were incubated in Protease III for 30 min at 40°C, followed by wash with dd H_2O. The sections were incubated with RNAscope probes—Mm-Slc17a6 (Vglut2), Mm-Slc32a1-C2 (Vgat) for 2 h at 40 °C, followed by amplifying hybridization processes (AMP1 and AMP2 for 30 min; AMP3 for 15 min). Finally, the HRP probes (HRP-C1, HRP-C2) were hybridized for 15 min at 40°C, followed by 30 min incubation with Opal fluorescent ligands (Opal 570, and Opal 690, 1:1500 dilution) for 30 min at 40°C sequentially. The HRP blocker was applied for 15 min at 40°C between each HRP probe hybridization. Finally, the sections were counterstained with DAPI for 30 s at RT, before placing the coverslips. Fluorescence images were acquired using a confocal microscope with a 10× objective.

Slice Recording—To examine the connectivity between PCG GABAergic and glutamatergic neurons, Vgat-Cre::Ai14 mice injected with AAV1-EF1α-DIO-hChR2 (H134R)-EYFP-WPRE in PCG were used for slice recording. To confirm the connectivity between PCG axons and VTA GABAergic neurons, Vgat-Cre::Ai14 mice injected with AAV1-hSyn-hChR2 (H134R)-EYFP in PCG were used for slice recording. After three weeks injections, the in vitro acute brain slice recording was performed. Animals were anesthetized by urethane and then decapitated and the brain was rapidly removed and immersed in an ice-cold dissection buffer (composition: 60 mM NaCl, 3 mM KCl, 1.25 mM NaH_2PO_4, 25 mM $NaHCO_3$, 115mM sucrose, 10 mM glucose, 7 mM MgCl2, 0.5 mM $CaCl_2$; saturated with 95% O_2 and 5% CO_2; pH= 7.4). The brain slices were coronally sectioned into 300-μm-thick sections with a vibratome (Leica VT1000s). Slices were allowed to recover for 30 min in a submersion chamber filled with the warmed (35 °C) ACSF (composition, 119 mM NaCl, 26.2 mM $NaHCO_3$, 11 mM glucose, 2.5 mM KCl, 2 mM $CaCl_2$, 2 mM $MgCl_2$, 1.2 mM NaH_2PO_4, 2 mM sodium pyruvate, 0.5 mM VC). PCG neurons labeled with tdTomato (Vgat-Cre-tdTomato mice), VTA GABAergic neurons labeled with tdTomato (Vgat-Cre-tdTomato mice) or surrounded by EYFP+ fibers were visualized under a fluorescence microscope (Olympus BX51 WI). Patch pipettes (resistance of ~4–5 MΩ) filled with a cesium-based internal solution (composition, 125 mM cesium gluconate, 5 mM TEA-Cl, 2 mM NaCl, 2 mM CsCl, 10 mM HEPES, 10 mM EGTA, 4 mM ATP, 0.3 mM GTP and 10 mM phosphocreatine, pH 7.25; 290 mOsm) were used for whole-cell recordings. Signals were recorded with an Axopatch 700B amplifier (Molecular Devices) under voltage-clamp mode at a holding voltage of −70 mV for excitatory currents, filtered at 2 kHz and sampled at 10 kHz. Tetrodotoxin (TTX, 1μM) and 4-aminopyridine

(4-AP) (1 mM) were added to the external solution for recording monosynaptic responses to blue light stimulation (5-ms pulse, power of 3 mW, 10–30 trials).

Histology, imaging and quantification—Following all experiments, the animals were deeply anesthetized under isoflurane and perfused transcardially with phosphate-buffered saline (PBS) followed by 4% PFA. The brain was removed and post-fixed with 4% PFA for 24 h at 4°C. It was coronally sectioned into 150-μm-thick sections with a vibratome (Leica Microsystems). The free-floating sections were first washed three times with PBS for 10 min each time. The sections were then stained with Nissl reagent (Deep red, Invitrogen) for 3 h at room temperature. Aluminum foil was used to shield the sections from light. All the slices were examined under a confocal microscope (Olympus FluoView FV1000). To quantify the relative density of axonal projections of PCG neurons in downstream structures, brain regions of interest were collected and imaged and scanned at 10× magnification with the same parameters (such as laser power, scan speed, auto gain and offset value). Fluorescence quantifications were performed using FIJI (ImageJ. 2.1.0, NIH) by converting the images into monochromatic. Intensity value of the interest brain regions (200 × 200 pixel) were normalized to the baseline value. Four sections were collected and averaged for each of brain structures. The fluorescence density for each target structure was normalized for each animal and averaged across the animal group.

QUANTIFICATION AND STATISTICAL ANALYSIS

Data Analysis—For multichannel optrode recordings, spike trains were sorted offline. The signals were filtered through a bandpass filter (0.3–3 kHz). The 16-channel probes were grouped into four tetrodes and then performed semiautomatic spike sorting by using Offline Sorter (Plexon) following our previous studies [38,104]. To identify the units driven directly by ChR2 activation, we analyzed the onset latency of spikes relative to the onset of light stimulation. Only spikes with latency < 3-ms were considered as being directly stimulated in this study. The average waveforms were computed and compared between LED-evoked and sensory-evoked spikes. For noise and air puff response quantification, the Z-score was calculated as the firing rate (calculated within a 100-ms window after the stimulus onset) divided by the standard deviation of the baseline firing rate (calculated within a 50-ms window before the stimulus onset), with 1-ms bin. For sucrose response quantification, firing rates were normalized to the baseline activity by calculating a Z-score, with 10-ms bin [10], and for each cell, the evoked response within 2 s after the stimulus onset was compared.

Statistics—Shapiro–Wilk test was first used to examine whether samples had a normal distribution. In the case of a normal distribution, parametric tests were used. For two group comparison, significance was determined by using Student's *t*-test. Paired *t*-test was used to compare data from the same neuron or the same animal. One-way ANOVA followed by LSD or Tukey post hoc comparison was used for multiple comparisons. Significance level was marked as *: $P < 0.05$; **: $P < 0.01$; and ***: $P < 0.001$. Data are presented as mean ± SD, unless otherwise indicated. Statistical analysis was conducted using SPSS (IBM).

Supplementary Material

Refer to Web version on PubMed Central for supplementary material.

ACKNOWLEDGMENTS

This work was supported by grants from the U.S. National Institutes of Health (R01DC008983, RF1MH114112, MH116990 to L.I.Z.). H.W.T. was supported by NIH grants (EY019049, MH116990), and I.R.W. was supported by NIH BRAIN Initiative awards RF1MH120017, U01MH114829, and U19MH114830.

INCLUSION AND DIVERSITY

We support inclusive, diverse, and equitable conduct of research.

References

1. Etkin A Büchel C and Gross JJ (2015). The neural bases of emotion regulation. Nat Rev Neurosci. 16, 693–700. doi.org10.1038/nrn4044. [PubMed: 26481098]
2. LeDoux J (2012). Rethinking the emotional brain. Neuron 73, 653–676. doi.org10.1016/j.neuron.2012.02.004. [PubMed: 22365542]
3. Tye KM (2018). Neural Circuit Motifs in Valence Processing. Neuron 100, 436–452. doi.org10.1016/j.neuron.2018.10.001. [PubMed: 30359607]
4. Berridge KC (2019). Affective valence in the brain: modules or modes? Nat Rev Neurosci. 20, 225–234. doi.org10.1038/s41583-019-0122-8. [PubMed: 30718826]
5. Hu H (2016). Reward and Aversion. Annu Rev Neurosci. 39, 297–324. doi.org10.1146/annurev-neuro-070815-014106. [PubMed: 27145915]
6. Jennings JH Ung RL Resendez SL Stamatakis AM Taylor JG Huang J Veleta K Kantak PA Aita M Shilling-Scrivo K et al. (2015). Visualizing hypothalamic network dynamics for appetitive and consummatory behaviors. Cell 160, 516–527. doi.org10.1016/j.cell.2014.12.026. [PubMed: 25635459]
7. Jennings JH Rizzi G Stamatakis AM Ung RL and Stuber GD (2013). The inhibitory circuit architecture of the lateral hypothalamus orchestrates feeding. Science 341, 1517–1521. doi.org10.1126/science.1241812. [PubMed: 24072922]
8. Baker PM Jhou T Li B Matsumoto M Mizumori SJY Stephenson-Jones M and Vicentic A (2016). The Lateral Habenula Circuitry: Reward Processing and Cognitive Control. J Neurosci. 36, 11482–11488. doi.org10.1523/JNEUROSCI.2350-16.2016. [PubMed: 27911751]
9. Bromberg-Martin ES Matsumoto M and Hikosaka O (2010). Dopamine in motivational control: rewarding, aversive, and alerting. Neuron 68, 815–834. doi.org10.1016/j.neuron.2010.11.022. [PubMed: 21144997]
10. Shen L Zhang G-W Tao C Seo MB Zhang NK Huang JJ Zhang LI and Tao HW (2022). A bottom-up reward pathway mediated by somatostatin neurons in the medial septum complex underlying appetitive learning. Nat Commun. 13, 1194. doi.org10.1038/s41467-022-28854-z. [PubMed: 35256596]
11. Namburi P Al-Hasani R Calhoon GG Bruchas MR and Tye KM (2016). Architectural Representation of Valence in the Limbic System. Neuropsychopharmacology 41, 1697–1715. doi.org10.1038/npp.2015.358. [PubMed: 26647973]
12. Pignatelli M and Beyeler A (2019). Valence coding in amygdala circuits. Curr Opin Behav Sci. 26, 97–106. doi.org10.1016/j.cobeha.2018.10.010. [PubMed: 32832584]
13. Zhang X Guan W Yang T Furlan A Xiao X Yu K An X Galbavy W Ramakrishnan C Deisseroth K et al. (2021). Genetically identified amygdala–striatal circuits for valence-specific behaviors. Nat Neurosci. 24, 1586–1600. doi.org10.1038/s41593-021-00927-0. [PubMed: 34663958]
14. Cohen JY Haesler S Vong L Lowell BB and Uchida N (2012). Neuron-type-specific signals for reward and punishment in the ventral tegmental area. Nature 482, 85–88. doi.org10.1038/nature10754. [PubMed: 22258508]

15. Hikosaka O (2010). The habenula: from stress evasion to value-based decision-making. Nat Rev Neurosci. 11, 503–513. doi.org10.1038/nrn2866. [PubMed: 20559337]
16. Matsumoto M and Hikosaka O (2007). Lateral habenula as a source of negative reward signals in dopamine neurons. Nature 447, 1111–1115. doi.org10.1038/nature05860. [PubMed: 17522629]
17. Hu H Cui Y and Yang Y (2020). Circuits and functions of the lateral habenula in health and in disease. Nat Rev Neurosci. 21, 277–295. doi.org10.1038/s41583-020-0292-4. [PubMed: 32269316]
18. Berridge CW and Waterhouse BD (2003). The locus coeruleus-noradrenergic system: Modulation of behavioral state and state-dependent cognitive processes. Brain Res Rev. 42, 33–84. doi.org10.1016/S0165-0173(03)00143-7. [PubMed: 12668290]
19. Belova MA Paton JJ and Salzman CD (2008). Moment-to-moment tracking of state value in the amygdala. J Neurosci. 28, 10023–10030. doi.org10.1523/JNEUROSCI.1400-08.2008. [PubMed: 18829960]
20. Paton JJ Belova MA Morrison SE and Salzman CD (2006). The primate amygdala represents the positive and negative value of visual stimuli during learning. Nature 439, 865–870. doi.org10.1038/nature04490. [PubMed: 16482160]
21. Morrison SE and Salzman CD (2009). The convergence of information about rewarding and aversive stimuli in single neurons. J Neurosci. 29, 11471–11483. doi.org10.1523/JNEUROSCI.1815-09.2009. [PubMed: 19759296]
22. Phelps EA and LeDoux JE (2005). Contributions of the amygdala to emotion processing: from animal models to human behavior. Neuron 48, 175–187. doi.org10.1016/j.neuron.2005.09.025. [PubMed: 16242399]
23. Etkin A Egner T and Kalisch R (2011). Emotional processing in anterior cingulate and medial prefrontal cortex. Trends Cogn Sci. 15, 85–93. doi.org10.1016/j.tics.2010.11.004. [PubMed: 21167765]
24. Chikazoe J Lee DH Kriegeskorte N and Anderson AK (2014). Population coding of affect across stimuli, modalities and individuals. Nat Neurosci. 77, 1114–1122. doi.org10.1038/nn.3749.
25. Clithero JA and Rangel A (2014). Informatic parcellation of the network involved in the computation of subjective value. Soc Cogn Affect Neurosci. 9, 1289–1302. doi.org10.1093/scan/nst106. [PubMed: 23887811]
26. Cohen JY Amoroso MW and Uchida N (2015). Serotonergic neurons signal reward and punishment on multiple timescales. eLife 2015, 1–25. doi.org10.7554/eLife.06346.
27. Kim J Pignatelli M Xu S Itohara S and Tonegawa S (2016). Antagonistic negative and positive neurons of the basolateral amygdala. Nat Neurosci. 19, 1636–1646. doi.org10.1038/nn.4414. [PubMed: 27749826]
28. Kravitz AV Tye LD and Kreitzer AC (2012). Distinct roles for direct and indirect pathway striatal neurons in reinforcement. Nat Neurosci. 15, 816–818. doi.org10.1038/nn.3100. [PubMed: 22544310]
29. Schultz W Dayan P and Montague PR (1997). A neural substrate of prediction and reward. Science 275, 1593–1599. doi.org10.1126/science.275.5306.1593. [PubMed: 9054347]
30. Redondo RL Kim J Arons AL Ramirez S Liu X and Tonegawa S (2014). Bidirectional switch of the valence associated with a hippocampal contextual memory engram. Nature 513, 426–430. doi.org10.1038/nature13725. [PubMed: 25162525]
31. Lee TMC Sun D Wong NML Shao R Men W Ge J So KF Gao JH and Chan CCH (2015). A Pontine Region is a Neural Correlate of the Human Affective Processing Network. EBioMedicine 2, 1799–1805. doi.org10.1016/j.ebiom.2015.10.020. [PubMed: 26870804]
32. Wong JJ Chang DHF Qi D Men W Gao JH and Lee TMC (2020). The pontine-driven somatic gaze tract contributes to affective processing in humans. NeuroImage 213. doi.org10.1016/j.neuroimage.2020.116692.
33. Wong JJ Wong NML Chang DHF Qi D Chen L and Lee TMC (2022). Amygdala–pons connectivity is hyperactive and associated with symptom severity in depression. Commun Biol. 5. doi.org10.1038/s42003-022-03463-0.

34. Damasio AR Grabowski TJ Bechara A Damasio H Ponto LLB Parvizi J and Hichwa RD (2000). Subcortical and cortical brain activity during the feeling of self-generated emotions. Nat Neurosci. 3, 1049–1056. doi.org10.1038/79871. [PubMed: 11017179]
35. Boucetta S Cissé Y Mainville L Morales M and Jones BE (2014). Discharge profiles across the sleep-waking cycle of identified cholinergic, GABAergic, and glutamatergic neurons in the pontomesencephalic tegmentum of the rat. J Neurosci. 34, 4708–4727. doi.org10.1523/JNEUROSCI.2617-13.2014. [PubMed: 24672016]
36. Cox J Pinto L and Dan Y (2016). Calcium imaging of sleep-wake related neuronal activity in the dorsal pons. Nat Commun. 7, 1–7. doi.org10.1038/ncomms10763.
37. Zhang GW Sun WJ Zingg B Shen L He J Xiong Y Tao HW and Zhang LI (2018). A Non-canonical Reticular-Limbic Central Auditory Pathway via Medial Septum Contributes to Fear Conditioning. Neuron 97, 406–417.e4. doi.org10.1016/j.neuron.2017.12.010. [PubMed: 29290554]
38. Zhang GW Shen L Zhong W Xiong Y Zhang LI and Tao HW (2018). Transforming Sensory Cues into Aversive Emotion via Septal-Habenular Pathway. Neuron 99, 1016–1028.e5. doi.org10.1016/j.neuron.2018.07.023. [PubMed: 30122379]
39. Rahman M and Tadi P (2022). Neuroanatomy, Pons. In: StatPearls [Internet].
40. Abram SV Hua JPY and Ford JM (2022). Consider the pons: bridging the gap on sensory prediction abnormalities in schizophrenia. Trends Neurosci. 45, 798–808. doi.org10.1016/j.tins.2022.08.008. [PubMed: 36123224]
41. Lecca S Meye FJ Trusel M Tchenio A Harris J Schwarz MK Burdakov D Georges F and Mameli M (2017). Aversive stimuli drive hypothalamus-to-habenula excitation to promote escape behavior. eLife 6, 1–16. doi.org10.7554/eLife.30697.
42. Stamatakis AM and Stuber GD (2013). Activation of lateral habenula inputs to the ventral midbrain promotes behavioral avoidance. Nat Neurosci. 15, 1105–1107. doi.org10.1038/nn.3145.
43. Gehrlach DA Dolensek N Klein AS Roy Chowdhury R Matthys A Junghänel M Gaitanos TN Podgornik A Black TD Reddy Vaka N et al. (2019). Aversive state processing in the posterior insular cortex. Nature Neuroscience 22, 1424–1437. doi.org10.1038/s41593-019-0469-1. [PubMed: 31455886]
44. Liu MY Yin CY Zhu LJ Zhu XH Xu C Luo CX Chen H Zhu DY and Zhou QG (2018). Sucrose preference test for measurement of stress-induced anhedonia in mice. Nat Protoc. 13, 1686–1698. doi.org10.1038/s41596-018-0011-z. [PubMed: 29988104]
45. Belova MA Paton JJ Morrison SE and Salzman CD (2007). Expectation Modulates Neural Responses to Pleasant and Aversive Stimuli in Primate Amygdala. Neuron 55, 970–984. doi.org10.1016/j.neuron.2007.08.004. [PubMed: 17880899]
46. Bradley MM Miccoli L Escrig MA and Lang PJ (2008). The pupil as a measure of emotional arousal and autonomic activation. Psychophysiology 45, 602–607. doi.org10.1111/j.1469-8986.2008.00654.x. [PubMed: 18282202]
47. Bradshaw J (1967). Pupil size as a measure of arousal during information processing. Nature 216, 515–516. doi.org10.1038/216515a0. [PubMed: 6057275]
48. Reimer J McGinley MJ Liu Y Rodenkirch C Wang Q McCormick DA and Tolias AS (2016). Pupil fluctuations track rapid changes in adrenergic and cholinergic activity in cortex. Nat Commun. 7, 1–7. doi.org10.1038/ncomms13289.
49. Wang C-A Boehnke SE Itti L and Munoz DP (2014). Transient pupil response is modulated by contrast-based saliency. J Neurosci. 34, 408–417. doi.org10.1523/JNEUROSCI.3550-13.2014. [PubMed: 24403141]
50. Lu L Ren Y Yu T Liu Z Wang S Tan L Zeng J Feng Q Lin R Liu Y et al. (2020). Control of locomotor speed, arousal, and hippocampal theta rhythms by the nucleus incertus. Nat Commun. 11, 1–16. doi.org10.1038/s41467-019-14116-y. [PubMed: 31911652]
51. Liao HI Kidani S Yoneya M Kashino M and Furukawa S (2016). Correspondences among pupillary dilation response, subjective salience of sounds, and loudness. Psychon Bull Rev. 23, 412–425. doi.org10.3758/s13423-015-0898-0. [PubMed: 26163191]

52. Tsai H-C Zhang F Adamantidis A Stuber GD Bonci A de Lecea L and Deisseroth K (2009). Phasic firing in dopaminergic neurons is sufficient for behavioral conditioning. Science 324, 1080–1084. doi.org10.1126/science.1168878. [PubMed: 19389999]
53. Zhang F Tsai HC Airan RD Stuber GD Adamantidis AR De Lecea L Bonci A and Deisseroth K (2015). Optogenetics in freely moving mammals: Dopamine and reward. Cold Spring Harb Protoc., 715–724. doi.org10.1101/pdb.top086330. [PubMed: 26240415]
54. Li Y Zhong W Wang D Feng Q Liu Z Zhou J Jia C Hu F Zeng J Guo Q et al. (2016). Serotonin neurons in the dorsal raphe nucleus encode reward signals. Nat Commun. 7. doi.org10.1038/ncomms10503.
55. Zhang GW Shen L Tao C Jung AH Peng B Li Z Zhang LI and Tao HW (2021). Medial preoptic area antagonistically mediates stress-induced anxiety and parental behavior. Nat Neurosci. 24, 516–528. doi.org10.1038/s41593-020-00784-3. [PubMed: 33526942]
56. Luo L Callaway EM and Svoboda K (2018). Genetic Dissection of Neural Circuits: A Decade of Progress. Neuron 98, 256–281. doi.org10.1016/j.neuron.2018.03.040. [PubMed: 29673479]
57. Tan KR Yvon C Turiault M Mirzabekov JJ Doehner J Labouèbe G Deisseroth K Tye KM and Lüscher C (2012). GABA Neurons of the VTA Drive Conditioned Place Aversion. Neuron 73, 1173–1183. doi.org10.1016/j.neuron.2012.02.015. [PubMed: 22445344]
58. Iglesias AG and Flagel SB (2021). The Paraventricular Thalamus as a Critical Node of Motivated Behavior via the Hypothalamic-Thalamic-Striatal Circuit. Front Integr Neurosci. 15, 706713. doi.org10.3389/fnint.2021.706713. [PubMed: 34220458]
59. Lavin TK Jin L Lea NE and Wickersham IR (2020). Monosynaptic Tracing Success Depends Critically on Helper Virus Concentrations. Front Synaptic Neurosci. 12, 6. doi.org10.3389/fnsyn.2020.00006. [PubMed: 32116642]
60. Liu K Kim J Kim DW Zhang YS Bao H Denaxa M Lim SA Kim E Liu C Wickersham IR et al. (2017). Lhx6-positive GABA-releasing neurons of the zona incerta promote sleep. Nature 548, 582–587. doi.org10.1038/nature23663. [PubMed: 28847002]
61. Weible AP Schwarcz L Wickersham IR Deblander L Wu H Callaway EM Seung HS and Kentros CG (2010). Transgenic targeting of recombinant rabies virus reveals monosynaptic connectivity of specific neurons. J Neurosci. 30, 16509–16513. doi.org10.1523/JNEUROSCI.2442-10.2010. [PubMed: 21147990]
62. Rolls ET (2000). The orbitofrontal cortex and reward. Cereb Cortex. 10, 284–294. doi.org10.1093/cercor/10.3.284. [PubMed: 10731223]
63. Wallis JD (2011). Cross-species studies of orbitofrontal cortex and value-based decision-making. Nat Neurosci. 15, 13–19. doi.org10.1038/nn.2956. [PubMed: 22101646]
64. Rolls ET Cheng W and Feng J (2020). The orbitofrontal cortex: reward, emotion and depression. Brain Commun. 2, fcaa196. doi.org10.1093/braincomms/fcaa196. [PubMed: 33364600]
65. Saez A Rigotti M Ostojic S Fusi S and Salzman CD (2015). Abstract Context Representations in Primate Amygdala and Prefrontal Cortex. Neuron 87, 869–881. doi.org10.1016/j.neuron.2015.07.024. [PubMed: 26291167]
66. McGaugh JL (2004). The amygdala modulates the consolidation of memories of emotionally arousing experiences. Annu Rev Neurosci. 27, 1–28. doi.org10.1146/annurev.neuro.27.070203.144157. [PubMed: 15217324]
67. Faget L Zell V Souter E McPherson A Ressler R Gutierrez-Reed N Yoo JH Dulcis D and Hnasko TS (2018). Opponent control of behavioral reinforcement by inhibitory and excitatory projections from the ventral pallidum. Nat Commun. 9, 1–14. doi.org10.1038/s41467-018-03125-y. [PubMed: 29317637]
68. Stephenson-Jones M Bravo-Rivera C Ahrens S Furlan A Xiao X Fernandes-Henriques C and Li B (2020). Opposing Contributions of GABAergic and Glutamatergic Ventral Pallidal Neurons to Motivational Behaviors. Neuron 105, 921–933.e5. doi.org10.1016/j.neuron.2019.12.006. [PubMed: 31948733]
69. Jennings JH Sparta DR Stamatakis AM Ung RL Pleil KE Kash TL and Stuber GD (2013). Distinct extended amygdala circuits for divergent motivational states. Nature 496, 224–228. doi.org10.1038/nature12041. [PubMed: 23515155]

70. Goto M Swanson LW and Canteras NS (2001). Connections of the nucleus incertus. J Comp Neurol. 438, 86–122. doi.org10.1002/cne.1303. [PubMed: 11503154]
71. Yeomans JS Li L Scott BW and Frankland PW (2002). Tactile, acoustic and vestibular systems sum to elicit the startle reflex. Neurosci Biobehav Rev. 26, 1–11. doi.org10.1016/s0149-7634(01)00057-4. [PubMed: 11835980]
72. Koch M and Schnitzler HU (1997). The acoustic startle response in rats--circuits mediating evocation, inhibition and potentiation. Behav Brain Res. 89, 35–49. doi.org10.1016/s0166-4328(97)02296-1. [PubMed: 9475613]
73. Protopopescu X Pan H Altemus M Tuescher O Polanecsky M McEwen B Silbersweig D and Stern E (2005). Orbitofrontal cortex activity related to emotional processing changes across the menstrual cycle. Proc Natl Acad Sci U S A. 102, 16060–16065. doi.org10.1073/pnas.0502818102. [PubMed: 16247013]
74. Anderson DJ and Adolphs R (2014). A framework for studying emotions across species. Cell 157, 187–200. doi.org10.1016/j.cell.2014.03.003. [PubMed: 24679535]
75. Wikenheiser AM and Schoenbaum G (2016). Over the river, through the woods: cognitive maps in the hippocampus and orbitofrontal cortex. Nat Rev Neurosci. 17, 513–523. doi.org10.1038/nrn.2016.56. [PubMed: 27256552]
76. McLaughlin I Dani JA and De Biasi M (2017). The medial habenula and interpeduncular nucleus circuitry is critical in addiction, anxiety, and mood regulation. J Neurochem. 142 Suppl, 130–143. doi.org10.1111/jnc.14008. [PubMed: 28791703]
77. Herkenham M and Nauta WJ (1979). Efferent connections of the habenular nuclei in the rat. J Comp Neurol. 187, 19–47. doi.org10.1002/cne.901870103. [PubMed: 226566]
78. Hikosaka O Sesack SR Lecourtier L and Shepard PD (2008). Habenula: crossroad between the basal ganglia and the limbic system. J Neurosci. 28, 11825–11829. doi.org10.1523/JNEUROSCI.3463-08.2008. [PubMed: 19005047]
79. McGovern DJ Polter AM and Root DH (2021). Neurochemical Signaling of Reward and Aversion to Ventral Tegmental Area Glutamate Neurons. J Neurosci. 41, 5471–5486. doi.org10.1523/JNEUROSCI.1419-20.2021. [PubMed: 34001626]
80. Ouhaz Z Fleming H and Mitchell AS (2018). Cognitive functions and neurodevelopmental disorders involving the prefrontal cortex and mediodorsal thalamus. Front Neurosci. 12, 1–18. doi.org10.3389/fnins.2018.00033. [PubMed: 29403346]
81. Collins DP Anastasiades PG Marlin JJ and Carter AG (2018). Reciprocal Circuits Linking the Prefrontal Cortex with Dorsal and Ventral Thalamic Nuclei. Neuron 98, 366–379.e4. doi.org10.1016/j.neuron.2018.03.024. [PubMed: 29628187]
82. Oddie SD and Bland BH (1998). Hippocampal formation theta activity and movement selection. Neurosci Biobehav Rev. 22, 221–231. doi.org10.1016/s0149-7634(97)00003-1. [PubMed: 9579313]
83. Müller C and Remy S (2018). Septo-hippocampal interaction. Cell Tissue Res. 373, 565–575. doi.org10.1007/s00441-017-2745-2. [PubMed: 29250747]
84. Vann SD and Nelson AJD (2015). The mammillary bodies and memory: more than a hippocampal relay. Prog Brain Res. 219, 163–185. doi.org10.1016/bs.pbr.2015.03.006. [PubMed: 26072239]
85. Roseberry TK Lee AM Lalive AL Wilbrecht L Bonci A and Kreitzer AC (2016). Cell-Type-Specific Control of Brainstem Locomotor Circuits by Basal Ganglia. Cell 164, 526–537. doi.org10.1016/j.cell.2015.12.037. [PubMed: 26824660]
86. Andrade TG Zangrossi HJ and Graeff FG (2013). The median raphe nucleus in anxiety revisited. J Psychopharmacol. 27, 1107–1115. doi.org10.1177/0269881113499208. [PubMed: 23999409]
87. Szo A Zichó K Barth AM Gönczi RT Schlingloff D Török B Sipos E Major A Bardóczi Z Sos KE et al. (2019). Median raphe controls acquisition of negative experience in the mouse. Science 366. doi.org10.1126/science.aay8746.
88. Wang DV Yau HJ Broker CJ Tsou JH Bonci A and Ikemoto S (2015). Mesopontine median raphe regulates hippocampal ripple oscillation and memory consolidation. Nat Neurosci. 18, 728–735. doi.org10.1038/nn.3998. [PubMed: 25867120]

89. Lazaridis I Tzortzi O Weglage M Märtin A Xuan Y Parent M Johansson Y Fuzik J Fürth D Fenno LE et al. (2019). A hypothalamus-habenula circuit controls aversion. Mol Psychiatry. 24, 1351–1368. doi.org10.1038/s41380-019-0369-5. [PubMed: 30755721]

90. Barker DJ Miranda-Barrientos J Zhang S Root DH Wang HL Liu B Calipari ES and Morales M (2017). Lateral Preoptic Control of the Lateral Habenula through Convergent Glutamate and GABA Transmission. Cell Reports 21, 1757–1769. doi.org10.1016/j.celrep.2017.10.066. [PubMed: 29141211]

91. Root DH Estrin DJ and Morales M (2018). Aversion or Salience Signaling by Ventral Tegmental Area Glutamate Neurons. iScience 2, 51–62. doi.org10.1016/j.isci.2018.03.008. [PubMed: 29888759]

92. Matsumoto H Tian J Uchida N and Watabe-Uchida M (2016). Midbrain dopamine neurons signal aversion in a reward-context-dependent manner. eLife 5, 1–24. doi.org10.7554/eLife.17328.

93. Zhu Y Nachtrab G Keyes PC Allen WE Luo L and Chen X (2018). Dynamic salience processing in paraventricular thalamus gates associative learning. Science 362, 423–429. doi.org10.1126/science.aat0481. [PubMed: 30361366]

94. Oh SW Harris JA Ng L Winslow B Cain N Mihalas S Wang Q Lau C Kuan L Henry AM et al. (2014). A mesoscale connectome of the mouse brain. Nature 508, 207–214. doi.org10.1038/nature13186. [PubMed: 24695228]

95. Han X Chow BY Zhou H Klapoetke NC Chuong A Rajimehr R Yang A Baratta MV Winkle J Desimone R et al. (2011). A high-light sensitivity optical neural silencer: development and application to optogenetic control of non-human primate cortex. Front Syst Neurosci 5, 18. doi.org10.3389/fnsys.2011.00018. [PubMed: 21811444]

96. Gradinaru V Zhang F Ramakrishnan C Mattis J Prakash R Diester I Goshen I Thompson KR and Deisseroth K (2010). Molecular and cellular approaches for diversifying and extending optogenetics. Cell 141, 154–165. doi.org10.1016/j.cell.2010.02.037. [PubMed: 20303157]

97. Chen T-W Wardill TJ Sun Y Pulver SR Renninger SL Baohan A Schreiter ER Kerr RA Orger MB Jayaraman V et al. (2013). Ultrasensitive fluorescent proteins for imaging neuronal activity. Nature 499, 295–300. doi.org10.1038/nature12354. [PubMed: 23868258]

98. Dong HW (2008). The Allen reference atlas: A digital color brain atlas of the C57Bl/6J male mouse (John Wiley and Sons).

99. Zingg B Chou X-L Zhang Z-G Mesik L Liang F Tao HW and Zhang LI (2017). AAV-Mediated Anterograde Transsynaptic Tagging: Mapping Corticocollicular Input-Defined Neural Pathways for Defense Behaviors. Neuron 93, 33–47. doi.org10.1016/j.neuron.2016.11.045. [PubMed: 27989459]

100. Zingg B Peng B Huang J Tao HW and Zhang LI (2020). Synaptic Specificity and Application of Anterograde Transsynaptic AAV for Probing Neural Circuitry. J Neurosci. 40, 3250–3267. doi.org10.1523/JNEUROSCI.2158-19.2020. [PubMed: 32198185]

101. Zingg B Dong H-W Tao HW and Zhang LI (2022). Application of AAV1 for Anterograde Transsynaptic Circuit Mapping and Input-Dependent Neuronal Cataloging. Curr Protoc. 2, e339. doi.org10.1002/cpz1.339. [PubMed: 35044725]

102. Chou XL Wang X Zhang ZG Shen L Zingg B Huang J Zhong W Mesik L Zhang LI and Tao HW (2018). Inhibitory gain modulation of defense behaviors by zona incerta. Nat Commun. 9, 1–12. doi.org10.1038/s41467-018-03581-6. [PubMed: 29317637]

103. Chou XL Fang Q Yan L Zhong W Peng B Li H Wei J Tao HW and Zhang LI (2020). Contextual and cross-modality modulation of auditory cortical processing through pulvinar mediated suppression. eLife 9, 1–21. doi.org10.7554/eLife.54157.

104. Fang Q Chou X lin Peng B Zhong W Zhang LI and Tao HW (2020). A Differential Circuit via Retino-Colliculo-Pulvinar Pathway Enhances Feature Selectivity in Visual Cortex through Surround Suppression. Neuron 105, 355–369.e6. doi.org10.1016/j.neuron.2019.10.027. [PubMed: 31812514]

105. Liang F Xiong XR Zingg B Ji X Zhang LI and Tao HW (2015). Sensory Cortical Control of a Visually Induced Arrest Behavior via Corticotectal Projections. Neuron 86, 755–767. doi.org10.1016/j.neuron.2015.03.048. [PubMed: 25913860]

106. Vinck M Batista-Brito R Knoblich U and Cardin JA (2015). Arousal and Locomotion Make Distinct Contributions to Cortical Activity Patterns and Visual Encoding. Neuron 86, 740–754. doi.org10.1016/j.neuron.2015.03.028. [PubMed: 25892300]

107. Hintiryan H Hayes UL and Chambers KC (2006). Intraoral cheek fistulae: A refined technique. Lab Anim. 40, 456–464. doi.org10.1258/002367706778476479. [PubMed: 17018216]

108. Zhang G-W Shen L Li Z Tao HW and Zhang LI (2019). Track-Control, an automatic video-based real-time closed-loop behavioral control toolbox. bioRxiv, 2019.12.11.873372. doi.org10.1101/2019.12.11.873372.

109. Li Z Wei J-X Zhang G-W Huang JJ Zingg B Wang X Tao HW and Zhang LI (2021). Corticostriatal control of defense behavior in mice induced by auditory looming cues. Nat Commun. 12, 1–13. doi.org10.1038/s41467-021-21248-7. [PubMed: 33397941]

Highlights

- PCG glutamate and GABA neurons encode negative and positive valence respectively
- These neurons mediate aversion and appetitive behaviors respectively
- Input-output organizations of PCG glutamate and GABA neurons are characterized
- PCG relays valence information into a globally distributed network

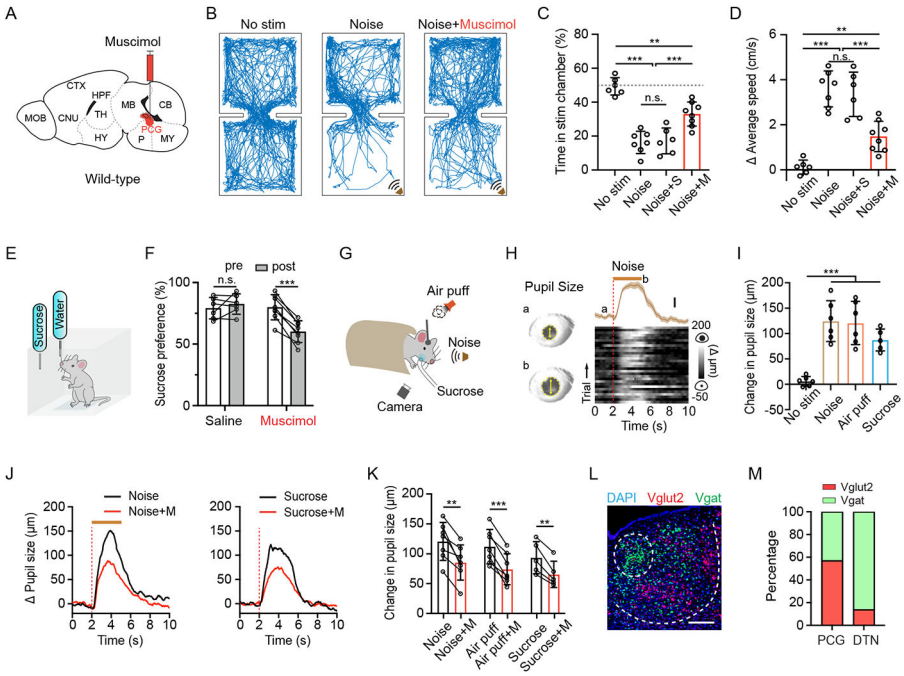

Figure 1. PCG mediates sensory-induced aversion and reward-related behavior.

(A) Schematic of a sagittal section of the mouse brain and infusion of fluorescent muscimol into PCG.

(B) Example movement tracking traces in the place preference test for three mice in no-stimulation, noise alone (80 dB SPL), and noise plus PCG silencing (with muscimol) conditions.

(C) Summary of percentage time spent in the stimulation chamber in different conditions. N = 6, 7, 6, 8 respectively. Gray dash line marks 50% level. **P < 0.01, ***P < 0.001, one-way ANOVA. “n.s.”, not significant. S, saline. M, muscimol.

(D) Summary of average locomotion speed in the stimulation chamber. N = 6, 7, 6, 8 respectively. **P < 0.01, ***P < 0.001, one-way ANOVA.

(E) Schematic of sucrose preference test.

(F) Summary of sucrose preference in the saline control and PCG silencing groups. N = 6 and 8 respectively. Sucrose preference was quantified as the relative amount of sucrose water consumption during a 1-hr test session (see Method). ***P < 0.001, paired *t*-test.

(G) Experimental configuration for measuring pupil size changes in responding to noise, air puffs or sucrose water (5%) delivery in awake head-fixed condition.

(H) Plot of pupil size changes in responding to noise (70 dB SPL, 3-s duration) for an example naïve animal. Left, example images of pupil during baseline (a) and dilated (b) conditions. Yellow arrows mark the pupil diameter. Right, plot of average change in pupil size (mean ± SEM) aligned to onset of noise stimulation (top) and Δ pupil size in each of 30 trials (bottom) for an example animal. Dotted red line indicates stimulus onset. Brown bar indicates the duration of noise.

(I) Summary of peak pupil size changes in no-stimulation, noise, air puffs and sucrose water delivery groups. N = 6, 6, 6, 5 respectively. ***P < 0.001, one-way ANOVA.

(J) Plot of average pupil size changes in responding to noise (left) or sucrose water (right) before (black) and after (red) silencing PCG with muscimol for an example mouse. Red dotted line indicates the onset time of stimulus. Brown bar indicates the duration of noise.
(K) Summary of peak pupil size changes in responding to different sensory stimuli before and after silencing PCG with muscimol. N = 7, 7, 5 respectively. **P < 0.01; ***P < 0.001, paired *t*-test.
(L) Representative RNAscope staining in PCG for the Vglut2 (red, Slc17a6) and Vgat (green, Slc32a1). Blue represents DAPI staining. Scale, 200 μm.
(M) Relative abundance of Vglut2+ (red) vs. Vgat+ (green) neurons. For each brain structure, n = 4 animals.
Error Bar = SD in all plots.

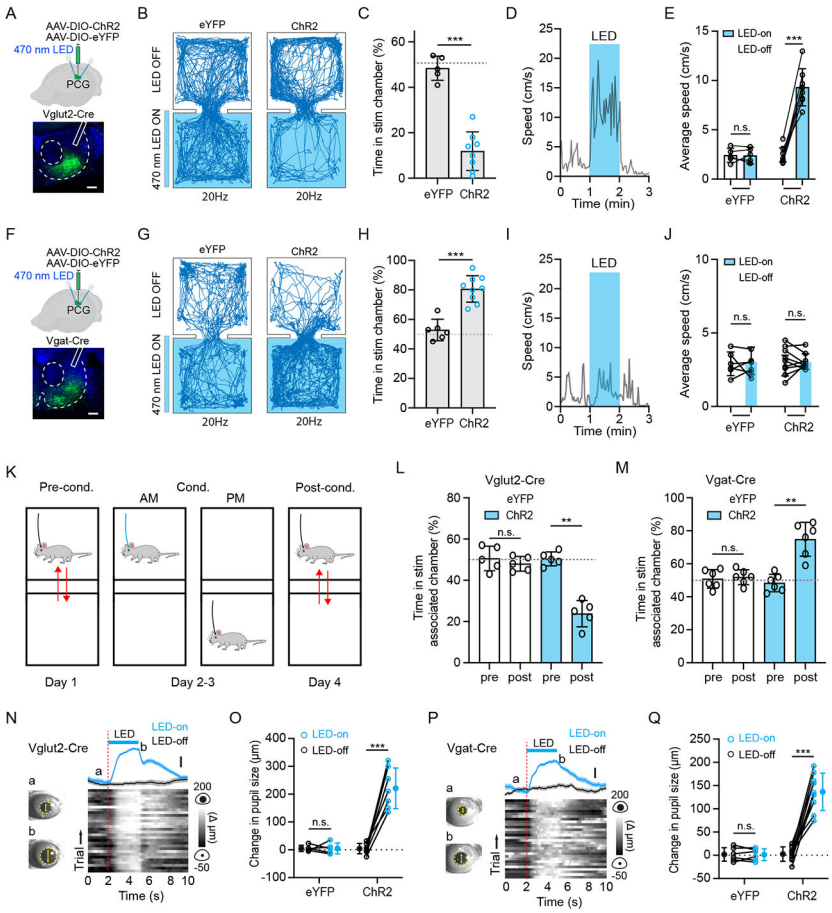

Figure 2. PCG glutamate and GABA neurons drive avoidance and preference behavior, respectively.

(A) Top, experimental condition; Bottom, representative confocal image showing the restricted expression of ChR2 within PCG. Scale, 200 μm.

(B) Example movement tracing for an animal in eYFP group or ChR2 group during a 20 min session of RTPP test with 20-Hz optical stimulation of PCG glutamatergic neurons.

(C) Percentage time spent in the LED-On chamber for the eYFP (n = 5) and ChR2 (n = 8) groups. Gray dash line marks 50% level. ***P < 0.001, *t*-test.

(D) Plot of locomotion speed in an open field test for an example animal. Blue box marks the duration of LED stimulation of PCG Vglut2+ neurons.

(E) Average speed in LED-On (1 min) and LED-Off epochs. N = 5 and 8 for the eYFP and ChR2 group, respectively. ***P < 0.001, paired *t*-test.

(F) Similar to (A) but for a Vgat-Cre mouse. Scale, 200 μm.

(G) Example movement tracing for a Vgat-Cre animal during a 20 min session of RTPP test with 20-Hz optical stimulation of PCG GABAergic neurons.

(H) Percentage time spent in the LED-On chamber for the eYFP (n = 6) and ChR2 (n = 9) groups. ***P < 0.001, *t*-test.

(I) Plot of locomotion speed in an open field test for an example Vgat-ChR2 animal.

(J) Average speed in LED-On (1 min) and LED-Off epochs. N = 6 and 9 respectively. P > 0.05, paired *t*-test.

(K) Timeline for CPA/CPP test.

(L and M) Percentage time spent in the LED-On chamber pre- and post-conditioning by activating PCG Vglut2+ neurons (L, n = 5 for each group) and Vgat+ neurons (M, n = 6 for each group). **P < 0.01, paired *t*-test.

(N) Plot of change in pupil size in responding to LED stimulation for an example Vglut2-Cre animal. Left, example images of pupil during baseline (a) and dilated (b) conditions. Right, plot of average change in pupil size (mean ± SEM) aligned to onset of optical stimulation (top) and Δ pupil size in each of 30 trials (bottom) for an example animal. Scale, 50 μm.

(O) Average change in pupil size in LED-On and LED-Off conditions. N = 5 and 7 respectively. ***P < 0.001, paired *t*-test.

(P) Plot of change in pupil size in responding to LED stimulation for an example Vgat-Cre animal. Scale, 50 μm.

(Q) Average change in pupil size in LED-On and LED-Off conditions. N = 6 and 9 respectively. ***P < 0.001, paired *t*-test.

Error Bar = SD in all plots.

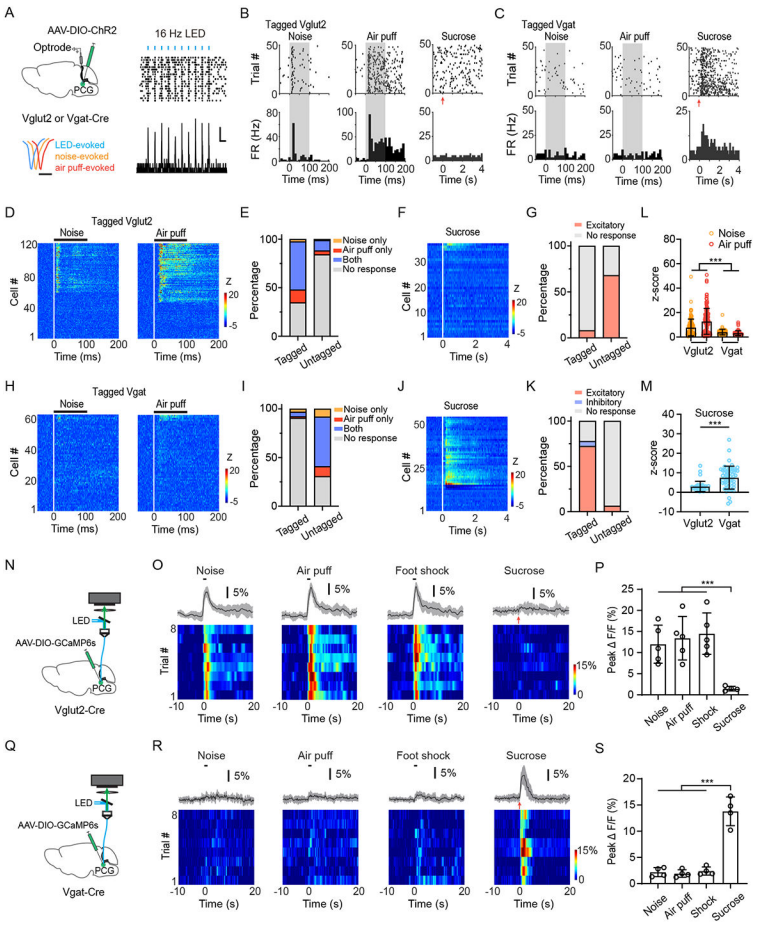

Figure 3. PCG glutamate and GABA neurons are activated preferentially by aversive and reward sensory signals, respectively.

(A) Left, schematic of optrode recording from ChR2-tagged PCG glutamatergic or GABAergic neurons (top) and average waveforms of LED-evoked (blue), noise-evoked (orange) and air-puff evoked (red) spikes from an example Vglut2+ unit (bottom). Scale, 0.5 ms. Right, raster plot (top) and peri-stimulus spike time histogram (PSTH, bottom) for LED-evoked spikes of an example tagged Vglut2+ neuron. Blue bars mark LED pulses (5-ms, 16 Hz). Scale, 5 Hz, 50 ms.

(B and C) Raster plot (top) and PSTH (bottom) for spike responses of an example PCG Vglut2+ neuron (B) or Vgat+ neuron (C) to 70 dB SPL noise (left), air puff (middle) and sucrose water delivery (right). Gray box marks the duration of sensory stimulation. Red arrows indicate the onset of sucrose water delivery.

(D) Heatmap plot of time-dependent Z score for spike responses of all tagged PCG Vglut2+ neurons (n = 121) to noise (left) or air puff (right). Each row represents a single neuron. The black bar above indicates the duration of the stimulation (onset is at time zero).

(E) Proportions of neurons activated by noise only, by air puff only, by both or by none in ChR2-tagged (n = 121) and untagged (n = 177) groups of Vglut2-Cre mice.

(F) Heatmap plot of time-dependent Z score for spike responses of all tagged PCG Vglut2+ neurons (n = 37) to sucrose water stimulation.

(G) Proportion of neurons activated by sucrose water delivery for tagged (n = 37) and untagged populations (n = 50).
(H) Heatmap plot of time-dependent Z score for spike responses of all recorded tagged Vgat+ units (n = 63) to 70 dB SPL white noise (left) or air puff (right).
(I) Proportions of neurons activated by noise only, by air puff only, by both or by none in ChR2-tagged (n = 63) and untagged (n = 49) groups of Vgat-Cre mice.
(J) Heatmap plot of Z-score for spikes of all recorded tagged Vgat+ units in response to sucrose consumption (n = 54).
(K) Proportions of neurons showing excitatory (light red), inhibitory (blue) or no (gray) responses to sucrose water in ChR2-tagged (n = 54) and untagged (n = 80) populations in Vgat-Cre mice.
(L) Comparison of the peak Z-score within a 100 ms window in responding to noise or air puff for tagged Vglut2+ (n = 121) and Vgat+ (n = 63) neurons. ***p < 0.001, one-way ANOVA.
(M) Comparison of the peak Z-score within a 0–2 s window in responding to sucrose water delivery for Vglut2+ (n = 37) and Vgat+ (n = 54) neurons. ***p < 0.001, *t*-test.
(N) Schematic of fiber photometry imaging from PCG Vglut2+ neurons.
(O) Top, average percentage fluorescence change (± SD) in responding to noise, air puffs, foot shocks, or sucrose water for an example Vglut2-Cre mouse. Bottom, heatmap of fluorescence change in all trials. Black bar indicates stimulus duration (1 s).
(P) Summary of peak fluorescence changes in responding to different stimuli in Vglut2-Cre mice. ***P < 0.001, one-way ANOVA, n = 5, 5, 5 and 4 from left to right.
(Q) Schematic of fiber photometry imaging from PCG Vgat+ neurons.
(R) Similar to (O) but for a Vgat-Cre mouse.
(S) Summary of fluorescence changes for Vgat-Cre mice. ***P < 0.001, one-way ANOVA, n = 4, 4, 4, and 4.
Error Bar = SD in all plots.

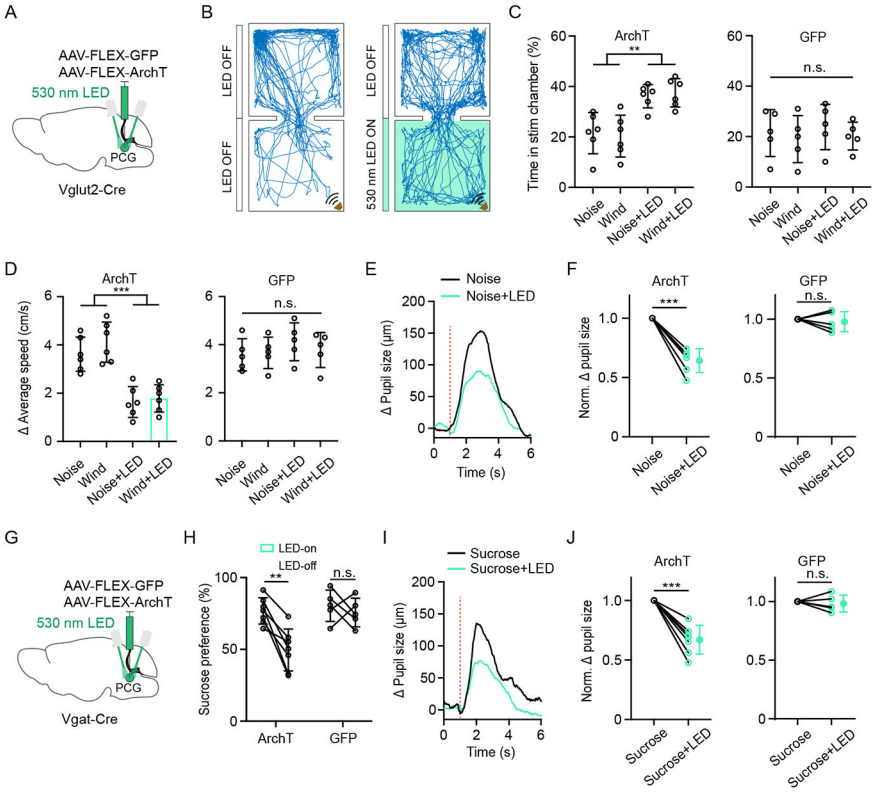

Figure 4. Effects of silencing PCG glutamate and GABA neurons on sensory-induced behaviors.

(A) Schematic viral injection for silencing PCG Vglut2+ neurons.

(B) Example movement tracking in RTPP test in noise stimulation (left) and noise plus green LED (right) condition.

(C) Summary of percentage time spent in the stimulation chamber in the ArchT (left, n = 6 for each subgroup) and GFP groups (right, n = 5 for each subgroup) under different conditions. **P < 0.01, one-way ANOVA.

(D) Summary of average speed increased in the stimulation chamber in the ArchT (left, n = 6 for each subgroup) and GFP groups (right, n = 5 for each subgroup) under different conditions. ***P < 0.001, one-way ANOVA.

(E) Average change in pupil size in responding to noise alone (black) and noise plus LED (green) for an example Vglut2-Cre mouse. Red dotted line indicates the stimulus onset.

(F) Comparison of normalized Δ pupil size increases between noise alone and noise plus LED conditions in ArchT (n = 6) and GFP (n = 5) groups. *** P < 0.001, paired *t*-test.

(G) Schematic viral injection for silencing PCG Vgat+ neurons.

(H) Summary of sucrose preference without and with LED illumination in the Arch T (n = 7) and GFP (n = 5) groups. **P < 0.01, paired *t*-test.

(I) Average pupil size changes in responding to sucrose alone (black line) and sucrose plus LED (green line) for an example mouse. Red dotted line indicates stimulus onset.

(J) Comparison of normalized Δ pupil size increases between sucrose alone and sucrose plus LED conditions in the ArchT (n = 7) and GFP (n = 5) groups. *** P < 0.001, paired *t*-test. Error Bar = SD in all plots.

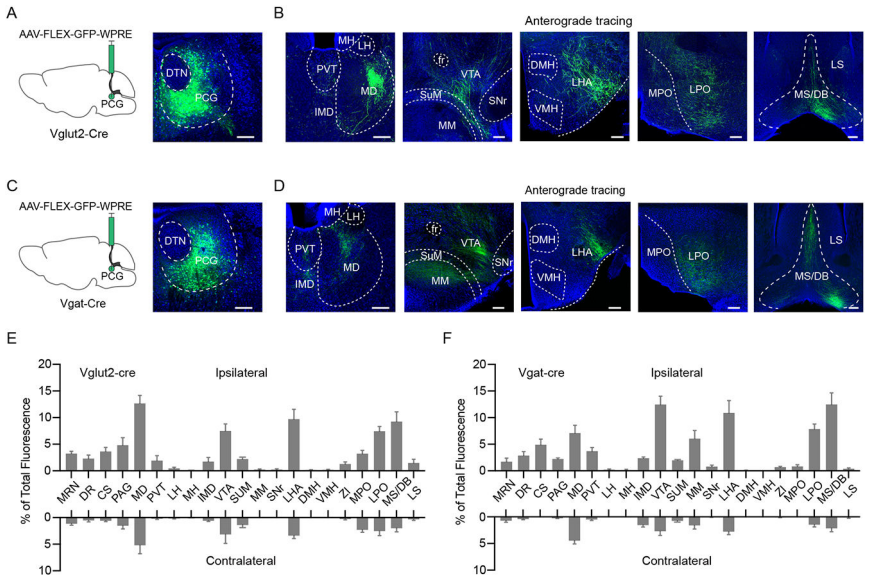

Figure 5. Projection targets of PCG glutamatergic and GABAergic neurons.

(A and B) Schematic viral injection (A, left panel) and fluorescence expression at the injection site (A, right panel) and GFP-labeled axons in major target regions (B) in a Vglut2-Cre mouse. Blue represents Nissl staining. Scale, 200 μm.

(C and D) Target regions of PCG Vgat+ axons in a Vgat-Cre mouse. Scale, 200 μm.

(E and F) Quantification of relative fluorescence density of GFP-labeled axons in different downstream regions of PCG Vglut2+ (E, n = 3 animals) and Vgat+ (F, n = 3 animals) neurons in the ipsilateral and contralateral side.

Error Bar = SD in all plots. Abbreviations: see Methods.

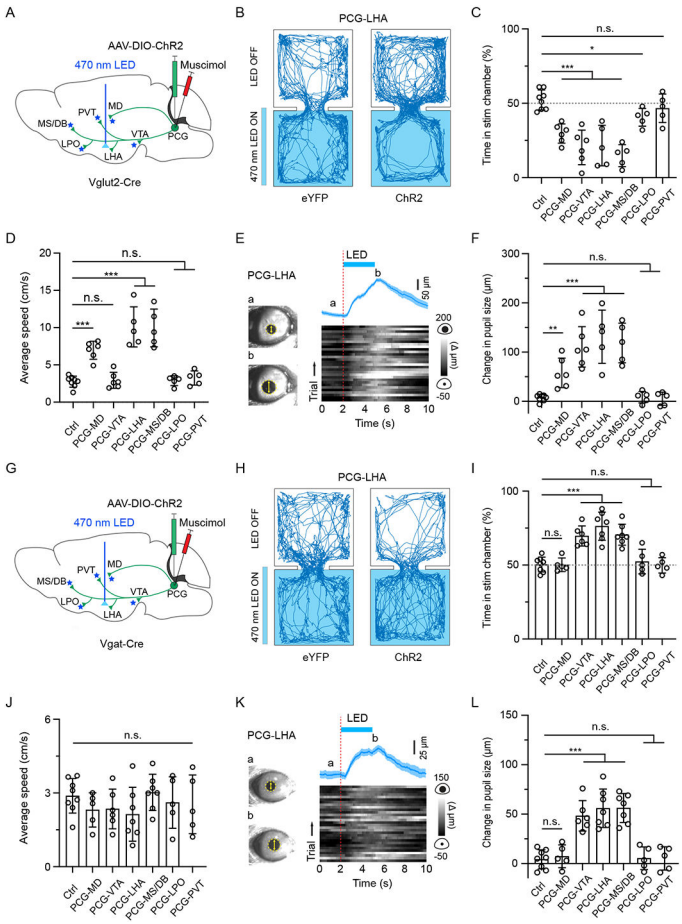

Figure 6. PCG glutamatergic and GABAergic neurons mediate behavioral effects through distinguishable downstream projections.

(A) Schematic viral injection and optical stimulation of PCG axon terminals in different target regions separately in Vglut2-Cre mice while silencing PCG cell bodies with muscimol.

(B) Movement tracking traces for an example eYFP and ChR2 animal in RTPP test with optical stimulation applied to PCG glutamatergic projections in LHA.

(C) Percentage time spent in the LED-On chamber with stimulation of PCG glutamatergic projections to different target regions. *P < 0.05, ***P < 0.001, one-way ANOVA; n = 8, 6, 6, 5, 5, 5 and 5 from left to right.

(D) Average locomotion speed during stimulation of PCG glutamatergic projections to different targets in the open field test. ***P < 0.001, one-way ANOVA; n = 8, 6, 6, 5, 5, 5 and 5 from left to right.

(E) Pupil size changes in responding to activation of PCG-to-LHA glutamatergic axons (30 trials) in an example animal. The trace on top represents as mean ± SEM.

(F) Summary of peak pupil size changes elicited by stimulating PCG glutamatergic projections to different targets. **P < 0.01, ***P < 0.001, one-way ANOVA; n = 8, 6, 6, 5, 5, 5 and 5 from left to right. Control mice were pooled.

(G) Similar to (A) but in Vgat-Cre mice.

(H) Movement tracking traces for an example animal in the RTPP test with optical stimulation applied to PCG GABAergic projections in LHA.
(I) Percentage time spent in the LED-On chamber with stimulation of PCG GABAergic projections to different target regions. ***P < 0.001, one-way ANOVA; n = 8, 5, 6, 7, 7, 5 and 5 from left to right.
(J) Average locomotion speed during stimulation of PCG GABAergic projections to different target regions in the open field test. P > 0.05, one-way ANOVA; n = 8, 5, 6, 7, 7, 5 and 5 from left to right.
(K) Pupil size changes in responding to activation of PCG-to-LHA GABAergic axons in an example animal.
(L) Summary of peak pupil size changes elicited by stimulating PCG GABAergic projections to different target regions. ***P < 0.001, one-way ANOVA; n = 8, 5, 6, 7, 7, 5 and 5 from left to right. Control mice were pooled.
Error Bar = SD in all plots.

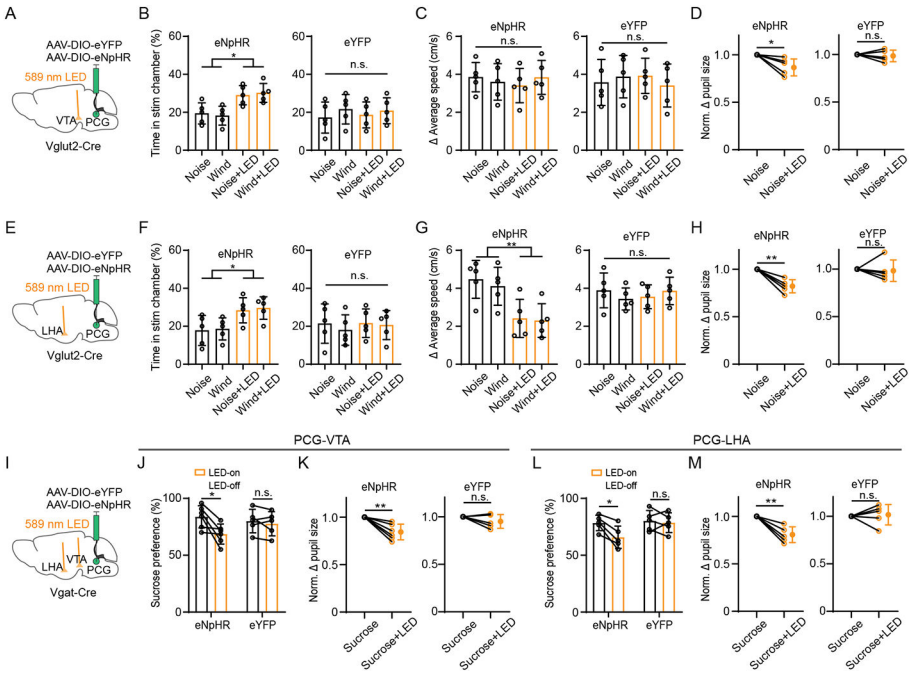

Figure 7. Silencing PCG glutamatergic and GABAergic projections to specific targets attenuates aversion and reward-related behavior, respectively.

(A) Optogenetic silencing (bilaterally) of PCG glutamatergic axon terminals in VTA.

(B) Summary of percentage time spent in the stimulation chamber in eNpHR (n = 5 for each subgroup) and eYFP (n = 5 for each subgroup) groups under different conditions. *P < 0.05, one-way ANOVA.

(C) Summary of increase in average speed in the stimulation chamber. P > 0.05, one-way ANOVA.

(D) Normalized Δ pupil size in noise alone and noise plus LED conditions in eNpHR (n = 5) and eYFP (n = 5) groups. * P < 0.05, paired *t*-test.

(E) Optogenetic silencing (bilaterally) of PCG glutamatergic axon terminals in LHA.

(F) Summary of percentage time spent in the stimulation chamber in the eNpHR (n = 5 for each subgroup) and eYFP (n = 5 for each subgroup) groups. *P < 0.05, one-way ANOVA.

(G) Summary of increase in average speed in the stimulation chamber in eNpHR (n = 5 for each subgroup) and eYFP (n = 5 for each subgroup) groups. **P < 0.01, one-way ANOVA.

(H) Normalized Δ pupil size in noise alone and noise plus LED conditions in eNpHR (n = 5) and eYFP (n = 5) groups. **P < 0.01, paired *t*-test.

(I) Optogenetic silencing of PCG GABAergic axon terminals in the LHA and VTA separately.

(J) Summary of sucrose preference without and with LED illumination in eNpHR (n = 6) and eYFP (n = 5) groups. *P < 0.05, paired *t*-test.

(K) Normalized Δ pupil size in sucrose alone and sucrose plus LED conditions in eNpHR (n = 6) and eYFP (n = 5) groups. **P < 0.01, paired *t*-test.

(L) Summary of sucrose preference without and with LED illumination in eNpHR (n = 5) and eYFP (n = 5) groups. *P < 0.05, paired *t*-test.

(M) Normalized Δ pupil size in sucrose alone and sucrose plus LED conditions in eNpHR (n = 5) and eYFP (n = 5) groups. **P < 0.01, paired *t*-test.

Error Bar = SD in all plots.

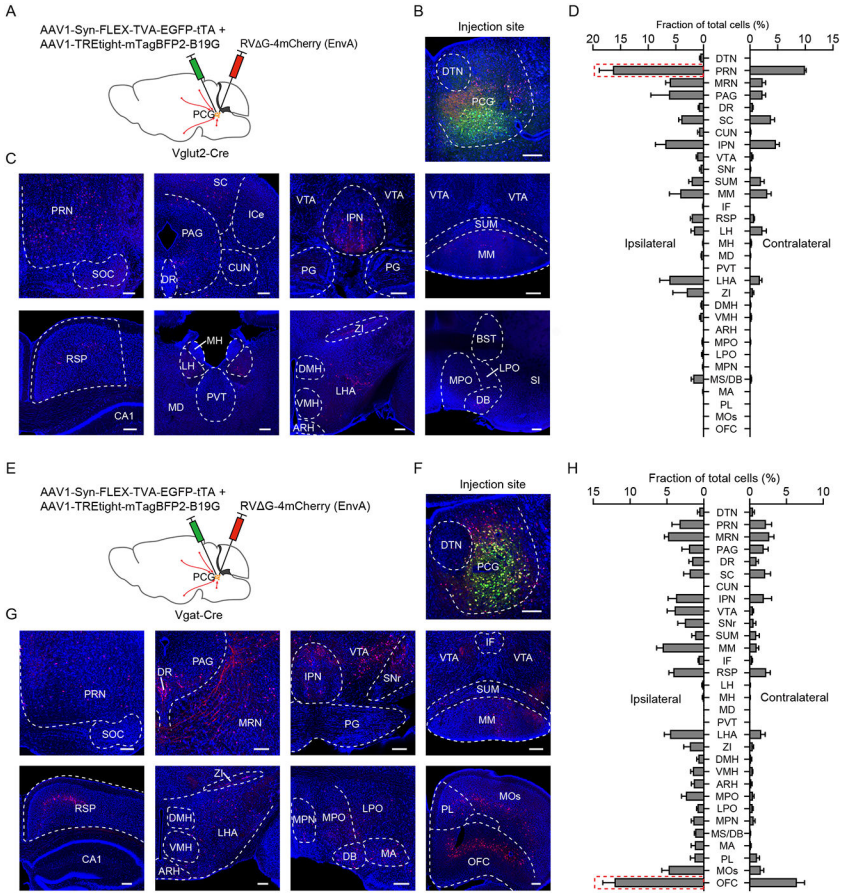

Figure 8. Monosynaptic inputs to PCG glutamatergic and GABAergic neurons.

(A) Strategy for cell-type specific retrograde tracing of monosynaptic inputs using pseudotyped rabies virus in Vglut2-Cre mice.

(B and C) Example images of fluorescence expression at the injection site (B) and in different input regions (C). Scale, 200 μm.

(D) Quantification of relative number of cells innervating PCG Vglut2+ neurons in different brain regions in the ipsilateral (left) and contralateral (right) side (n = 3; Bar = SD).

(E-H) Similar to (A-D) except for tracing of monosynaptic inputs to PCG Vgat+ neurons (n = 3). Scale, 200 μm.

Abbreviations: see Methods.

KEY RESOURCES TABLE

REAGENT or RESOURCE	SOURCE	IDENTIFIER
Antibodies		
Fluorescent Nissl Stain	Invitrogen	RRID: AB_2572212
RNAscope Mm-Slc17a6	ACDbio	Cat# 319171-C2
RNAscope Mm-Slc32a1	ACDbio	Cat# 319191-C3
Bacterial and Virus Strains		
AAV1-CAG-FLEX-GFP-WPRE	A gift from Hongkui Zeng[94]	Addgene plasmid # 51502
AAV1-EF1a-DIO-hChR2-eYFP	A gift from Karl Deisseroth	Addgene plasmid # 20298
AAV1-EF1a-DIO-eYFP	A gift from Karl Deisseroth	Addgene plasmid # 27056
AAV1-CAG-FLEX-ArchT-GFP	A gift from Edward Boyden[95]	Addgene plasmid # 29777
pAAV-hSyn-hChR2 (H134R)-EYFP	A gift from Karl Deisseroth	Addgene plasmid # 26973
pAAV-TREtight-mTagBFP2-B19G	A gift from Ian Wickersham[60]	Addgene plasmid # 100799
pAAV-Syn-FLEX-splitTVA-EGFP-tTA	A gift from Ian Wickersham[60]	Addgene plasmid # 100798
RVΔG-4mCherry (EnVA)	A gift from Ian Wickersham	N/A
pAAV-Ef1a-DIO-eNpHR-3.0-EYFP	A gift from Karl Deisseroth[96]	Addgene plasmid # 26966
AAV1-Syn-FLEX-GCamp6s-WPRE-SV40	A gift from Douglas Kim & GENIE Project[97]	Addgene plasmid # 100845
Chemicals, peptides, and recombinant proteins		
Kwik-Cast Sealant	WPI, Inc.	KWIK-CAST
Paraformaldehyde	Alfa Aesar OmniPur	10194340
NaCl	OmniPur	UI27FZEMS
KCl	Mallinckrodt	7447-40-7
$NaHCO_3$	EMD Chemicals	48204847
$MgCl_2$	J.T. Baker	7791-18-6
$CaCl_2$	EMD Chemicals	41046444
Glucose	Sigma	SLBC6575V
Sucrose	Millipore	D00168514
Agarose	OmniPur	3332C511
DAPI	ACDbio	323108
Dil	Invitrogen	D282
Muscimol,>98%; Tocris; 10mg	Fisher Scientific	28910
Experimental models: Organisms/strains		
Mouse: C57BL/6J	The Jackson Laboratory	RRID: IMSR_JAX:000664
Mouse: Ai14	The Jackson Laboratory	RRID: IMSR_JAX:007914
Mouse: VGluT2-ires-Cre mice	The Jackson Laboratory	RRID: IMSR_JAX: 016963
Mouse: VGAT-ires-Cre mice	The Jackson Laboratory	RRID: IMSR_JAX: 016962
Software and Algorithms		
Data acquisition with Labview	LabVIEW	http://www.ni.com/en-us/shop/labview.html: RRID: SCR_014325

REAGENT or RESOURCE	SOURCE	IDENTIFIER
Custom-written MATLAB code for analysis	MATLAB	http://www.mathworks.com/; RRID: SCR_001622
Allen Reference Atlas	(Dong, 2008)[98]	http://www.brainmap.org/; RRID: RRID: SCR_008848
Offline sorter	Plexon	http://plexon.com/;RRID: RRID: SCR_000012
Prism	GraphPad	https://www.graphpad.com/scientific-software/prism/; RRID:SCR_002798
Custom-written python code for analysis	Python	https://www.python.org/; RRID:SCR_008394
OpenCV library	OpenCV	https: opencv.org/;RRID: SCR_015526
Fiji	NIH	https://fiji.sc/; RRID:SCR_002285
Original code for analysis of behavioral data	https://doi.org/10.5281/zenodo.7604169	https://doi.org/10.5281/zenodo.7604169
Other		
Free Field Speaker	TDT MF1	N/A
Sound-Attenuation Booth	Gretch-Ken Industries	N/A
NI board for sound generation	National Instrument	PCl-6731
Microvalve	Lee Co.	LFAA1209512H
Optrode	Neuronexus Technologies	A1x16-Poly2-5mm-50 s-177-OA16LP